Article

Structure

Biophysical Characterization of the Tandem FHA Domain Regulatory Module from the *Mycobacterium tuberculosis* ABC Transporter Rv1747

Graphical Abstract

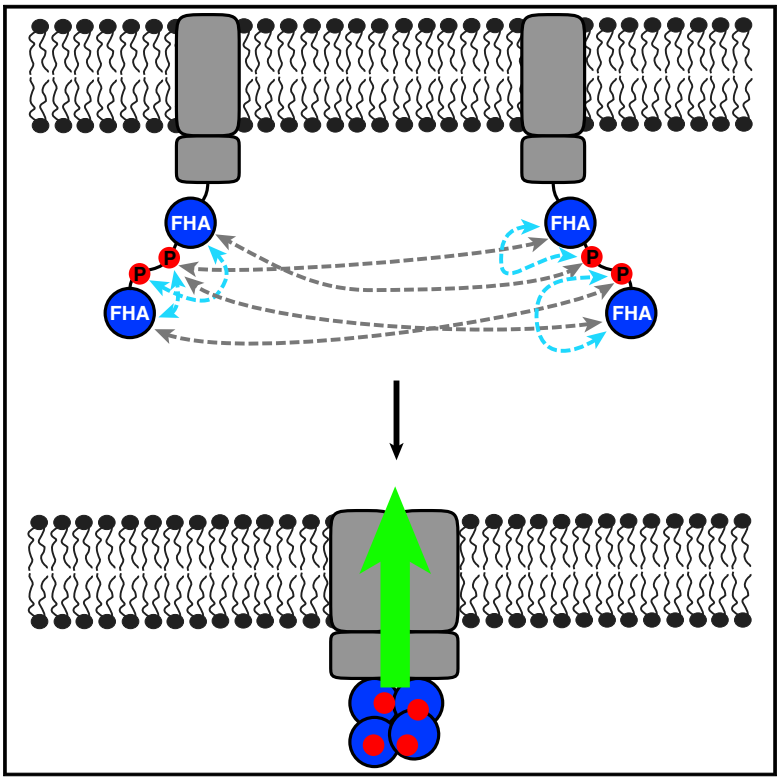

Highlights

- The ABC transporter Rv1747 has two cytoplasmic phosphothreonine-binding FHA domains
- FHA-2 is circularly permuted and more dynamic than the canonical β-sandwich FHA-1
- Both FHA domains bind either of two linker pThr via intra/intermolecular pathways
- Complex binding equilibria may enable tunable association and regulation of Rv1747

Authors

Florian Heinkel, Leo Shen, Melissa Richard-Greenblatt, ..., Yossef Av-Gay, Jörg Gsponer, Lawrence P. McIntosh

Correspondence

gsponer@msl.ubc.ca (J.G.), mcintosh@chem.ubc.ca (L.P.M.)

In Brief

Rv1747, a putative transporter of *Mtb* envelope components, has two cytoplasmic phosphothreonine-binding FHA domains joined by a disordered linker with two phospho-acceptor threonines. Heinkel et al. showed that both FHA domains bind either linker phosphothreonine intra- and intermolecularly with differing affinities. This could enable tunable Rv1747 regulation through phosphorylation-dependent oligomerization.

Heinkel et al., 2018, Structure *26*, 1–15
July 3, 2018
https://doi.org/10.1016/j.str.2018.04.018

CellPress

Please cite this article in press as: Heinkel et al., Biophysical Characterization of the Tandem FHA Domain Regulatory Module from the *Mycobacterium tuberculosis* ABC Transporter Rv1747, Structure (2018), https://doi.org/10.1016/j.str.2018.04.018

Structure
Article

Biophysical Characterization of the Tandem FHA Domain Regulatory Module from the *Mycobacterium tuberculosis* ABC Transporter Rv1747

Florian Heinkel,[1,2] Leo Shen,[3] Melissa Richard-Greenblatt,[4,5] Mark Okon,[3,6] Jennifer M. Bui,[2] Christine L. Gee,[7] Laurie M. Gay,[7] Tom Alber,[7,8] Yossef Av-Gay,[4,5] Jörg Gsponer,[2,3,*] and Lawrence P. McIntosh[2,3,6,9,*]
[1]Genome Science and Technology Program, University of British Columbia, Vancouver, BC V6T 1Z4, Canada
[2]Michael Smith Laboratories, University of British Columbia, Vancouver, BC V6T 1Z4, Canada
[3]Department of Biochemistry and Molecular Biology, University of British Columbia, Vancouver, BC V6T 1Z3, Canada
[4]Division of Infectious Diseases, Department of Medicine, University of British Columbia, Vancouver, BC V6H 3Z6, Canada
[5]Department of Microbiology and Immunology, University of British Columbia, Vancouver, BC V6T 1Z3, Canada
[6]Department of Chemistry, University of British Columbia, Vancouver, BC V6T 1Z1, Canada
[7]Department of Molecular and Cell Biology, University of California, Berkeley, CA 94720, USA
[8]Deceased
[9]Lead Contact
*Correspondence: gsponer@msl.ubc.ca (J.G.), mcintosh@chem.ubc.ca (L.P.M.)
https://doi.org/10.1016/j.str.2018.04.018

SUMMARY

The *Mycobacterium tuberculosis* ATP-binding cassette transporter Rv1747 is a putative exporter of cell wall biosynthesis intermediates. Rv1747 has a cytoplasmic regulatory module consisting of two pThr-interacting Forkhead-associated (FHA) domains connected by a conformationally disordered linker with two phospho-acceptor threonines (pThr). The structures of FHA-1 and FHA-2 were determined by X-ray crystallography and nuclear magnetic resonance (NMR) spectroscopy, respectively. Relative to the canonical 11-strand β-sandwich FHA domain fold of FHA-1, FHA-2 is circularly permuted and lacking one β-strand. Nevertheless, the two share a conserved pThr-binding cleft. FHA-2 is less stable and more dynamic than FHA-1, yet binds model pThr peptides with moderately higher affinity (~50 μM versus 500 μM equilibrium dissociation constants). Based on NMR relaxation and chemical shift perturbation measurements, when joined within a polypeptide chain, either FHA domain can bind either linker pThr to form intra- and intermolecular complexes. We hypothesize that this enables tunable phosphorylation-dependent multimerization to regulate Rv1747 transporter activity.

INTRODUCTION

Mycobacterium tuberculosis (*Mtb*), the etiological agent of tuberculosis, has elaborate strategies to circumvent host defense mechanisms. These strategies rely in part on an intricate stimulus-response system that has a set of 11 serine/threonine protein kinases (STPKs) as its central players (Chao et al., 2010; Wu et al., 2017). Several substrates of these STPKs contain a Forkhead-associated (FHA) domain (Grundner et al., 2005). This is a widespread phosphothreonine (pThr)-recognition module, found in eubacteria and eukaryotes, that mediates phosphorylation-dependent protein-protein interactions (Liang and Van Doren, 2008; Mahajan et al., 2008).

One of the FHA domain-containing substrates of the *Mtb* STPKs is an ATP-binding cassette (ABC) transporter encoded by the open reading frame *Rv1747* (Figure 1). Rv1747 has the single polypeptide chain topology expected for a homodimeric exporter with an N-terminal cytoplasmic nucleotide binding domain (NBD), the location of ATP hydrolysis, followed by a helical transmembrane domain through which substrate is transported (Braibant et al., 2000). Uniquely, the NBD of Rv1747 is preceded by a postulated regulatory module consisting of two FHA domains (FHA-1 and FHA-2) connected by an ~100 residue intrinsically disordered (ID) linker. The FHA domains are required for specific interactions with Rv1747's "cognate" STPK PknF (Molle et al., 2004) and likely with other *Mtb* STPKs (Grundner et al., 2005). PknF is considered Rv1747's cognate kinase because the two are encoded by the same operon. PknF phosphorylates the ID linker on least at two confirmed acceptor sites (T152 and T210), and short synthetic peptides corresponding to phosphorylated pT152 or pT210 can bind either of the isolated FHA domains with micromolar affinities (Spivey et al., 2011).

The exact functions of Rv1747 have not yet been elucidated. However, four of the remaining five *Mtb* proteins with FHA domains are involved in processes connected to cell wall synthesis or remodeling (Pallen et al., 2002). Also, experiments on *Rv1747* knockout strains revealed altered *Mtb* sedimentation phenotypes, decreased levels of phosphatidyl-*myo*-inositol mannosides in lipid extracts (Glass et al., 2017), and increased expression of the efflux pump-related *iniBAC* operon (Spivey et al., 2013). Collectively, these data link Rv1747 with the transport of cell wall biosynthesis intermediates. Most importantly, Rv1747 function is associated with *Mtb* infectivity. The

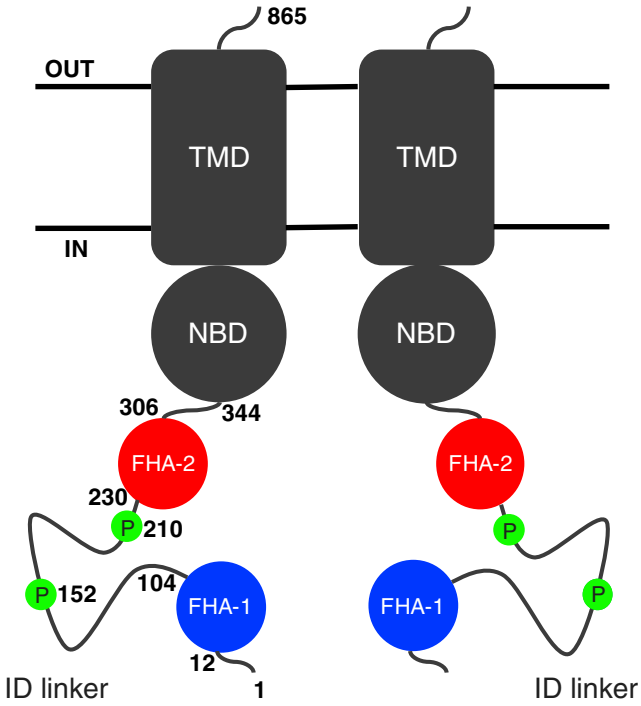

Figure 1. Architecture of the ABC Transporter Rv1747

Rv1747 contains a postulated cytoplasmic regulatory module composed of the FHA-1 (blue) and FHA-2 (red) domains joined by an ID linker with phospho-acceptor sites T152 and T210 (green).

ΔRv1747 mutant shows significantly attenuated growth in macrophages and mice (Curry et al., 2005; Glass et al., 2017). Similarly, strains with the phosphor-ablative T152A/T210A mutations exhibit reduced growth in macrophages and mice, and those with a mutation in the canonical pThr-binding site of FHA-1 have impaired growth in macrophages (Spivey et al., 2011). Thus the functions of Rv1747 are phosphorylation dependent, but very little is currently known about the roles played by the regulatory module.

Here, we investigate the structural and functional features of the Rv1747 regulatory module using a combination of nuclear magnetic resonance (NMR) spectroscopy, X-ray crystallography, isothermal titration calorimetry (ITC), and molecular dynamics (MD) simulations. The two FHA domains are structurally independent and joined by a flexible linker ("beads on a string"). FHA-1 has the canonical 11-strand β-sandwich fold of an FHA domain. In contrast, FHA-2 possesses an unusual, circularly permutated topology lacking one β-strand. FHA-2 is also more dynamic and less stable than FHA-1, yet binds pThr-containing peptides with higher affinity. Constructs of Rv1747 containing either FHA domain and the ID linker with either or both phospho-acceptor threonines exhibit inter- and intramolecular modes of FHA-pThr binding. This enables a complex interaction network that leads to higher order oligomerization of the full regulatory module upon phosphorylation. We hypothesize that association of the regulatory module can be fine-tuned based on the degree and sites of phosphorylation, and that this in turn modulates assembly or activation of Rv1747.

RESULTS

Rv1747 Regulatory Module Is Composed of Independent FHA-1 and FHA-2 Domains Joined by a Disordered Linker

We initially focused on three non-phosphorylated constructs: residues 1–156 ($Rv1747^{1-156}$) corresponding to the FHA-1 domain and part of the following interdomain linker; residues 206–310 ($Rv1747^{206-310}$) corresponding to the FHA-2 domain and a small part of the preceding linker; and residues 1–310 ($Rv1747^{1-310}$) spanning the entire regulatory module (Figure 2A). The assigned ^{15}N heteronuclear single quantum correlation (HSQC) spectra of the first two constructs showed dispersed cross-peaks attributed to the well-ordered regions of the FHA domains and more intense, sharper peaks with random coil $^{1}H^{N}$ chemical shifts of ~8–8.5 ppm originating from linker residues (Figures 2B and S1). Consistent with this interpretation, an analysis of the mainchain ^{1}H, ^{13}C, and ^{15}N chemical shifts with the MICS algorithm (Shen and Bax, 2012) indicated the presence of folded domains that are rich in β-strands (Figure 2C). In addition to lacking any predominant secondary structure, the linker residues exhibited MICS-calculated random coil index squared order parameters (RCI-S^2) indicative of conformational disorder. The presence of ordered FHA domains and ID linker residues is corroborated by amide ^{15}N relaxation (Figure S2) and hydrogen exchange (HX) experiments, discussed below.

The dispersed, assigned signals arising from the ordered domains in the ^{15}N-HSQC spectra of the FHA-1 and FHA-2 constructs overlap closely with those in the spectrum of the full regulatory module (Figure 2C). Based on the lack of amide chemical shift perturbations, it can be inferred that the two folded FHA domains do not interact when joined into a continuous non-phosphorylated polypeptide. Collectively, these data demonstrate that the Rv1747 regulatory module has a beads-on-a-string organization with two structurally independent FHA domains joined by an ID linker.

FHA-1 Has a Canonical FHA Domain Topology whereas FHA-2 Is Circularly Permuted

We determined the structure of FHA-1 ($Rv1747^{3-116}$) by X-ray crystallography (Figure 3A and Table 1) and the tertiary structural ensemble of FHA-2 ($Rv1747^{206-310}$) using NMR spectroscopy (Figure 3B and Table 2). FHA-1 has the canonical FHA domain topology with 11 β-strands in a β-sandwich fold and a shallow pThr-binding cleft extending across its apical surface. FHA-2 also has the expected two-sheet β-sandwich fold of an FHA domain. However, the canonical architecture exhibited by FHA-1 involves a six-stranded anti-parallel β-sheet (strands 2, 1, 11, 10, 7, 8) and five-stranded mixed β-sheet (4, 3, 5, 6, 9) (Liang and Van Doren, 2008). In contrast, FHA-2 is circularly permuted such that an additional C-terminal strand, denoted 1*, adopts the position of strand 1 in the first sheet. Also, the equivalent of strand 2 is missing, and thus the anti-parallel β-sheet only has five strands (1*, 11, 10, 7, 8). The permutation and the absence of strand 2 is particularly interesting as it places the T210 phospho-acceptor within the unstructured linker N-terminal to FHA-2. In a hypothetical homology model of this domain without the circular permutation, T210 would be part of

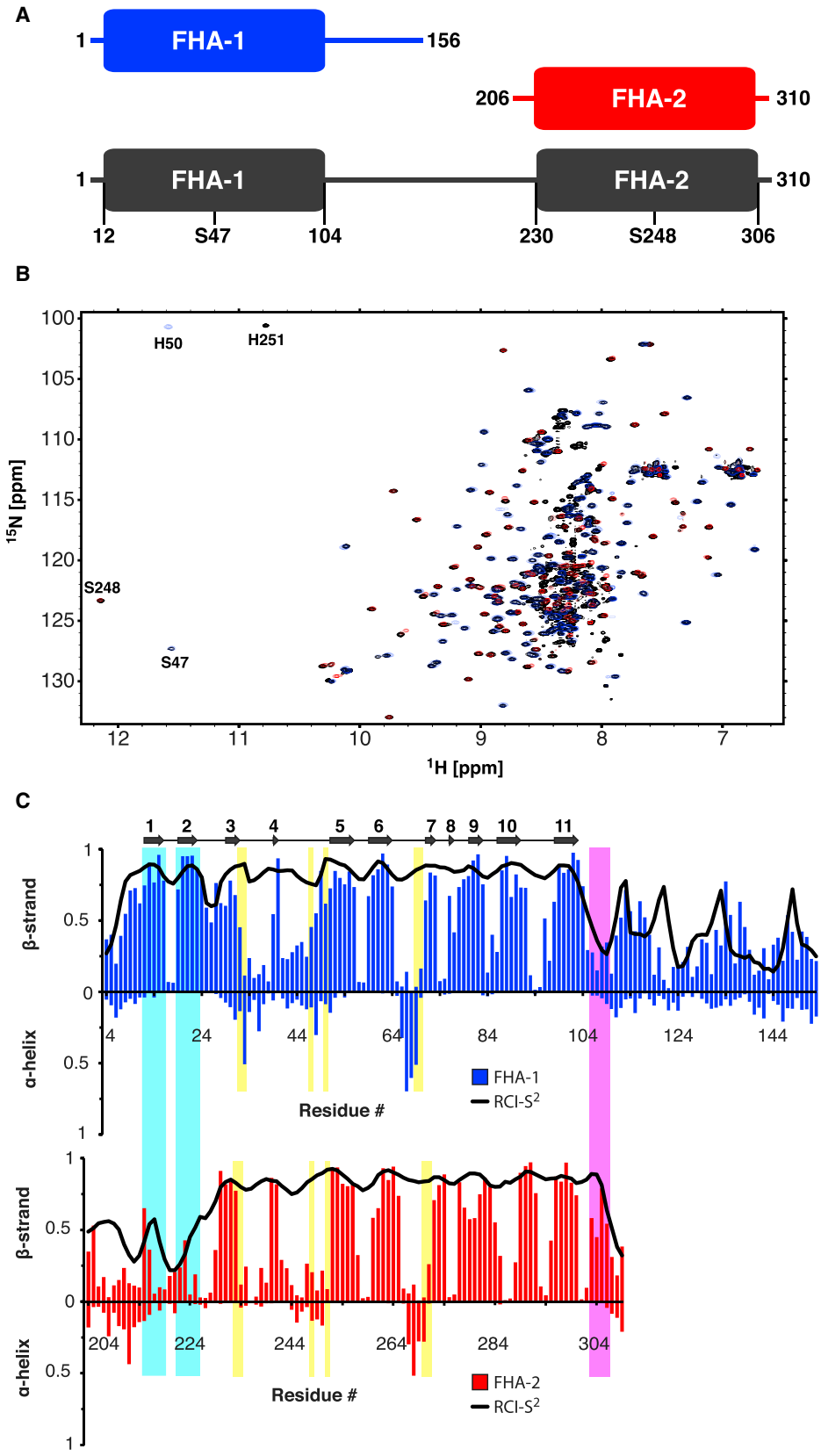

(legend on next page)

strand 2 and thus likely inaccessible for modification by the *Mtb* kinases and for FHA domain binding.

Despite significant sequence differences between FHA-1 and FHA-2 (27% identity, 36% similarity), as well as the circular permutation of FHA-2 and the absence of one β-strand, the two FHA domains have very similar overall tertiary structures (backbone root-mean-square deviation = 1.4 Å; Figure S3A). Importantly, residues that have been shown to be involved in phosphothreonine peptide binding by canonical FHA domains are conserved in sequence and structure (R33, S47, and H50 in FHA-1; R234, S248, and H251 in FHA-2; Figures 3C, 3D, and S3B). Furthermore, a hydrogen bond network supporting the binding site that is distinctive for FHA domains is present in both FHA-1 and FHA-2. This is readily seen by the characteristic (Mahajan et al., 2008) downfield amide $^{1}H^{N}$ chemical shifts of S47/S248 (11.58 ppm and 12.15 ppm), which reflect the formation of a hydrogen bond to the deprotonated $N^{\delta1}$ in the neutral H50/H251 sidechains of FHA-1/2, respectively. In turn, the nitrogen-bonded $H^{\varepsilon2}$ on these imidazole rings hydrogen bond to the backbone carbonyl of G71/G271. This protects the labile $^{1}H^{\varepsilon2}$ from rapid hydrogen exchange, yielding detectable signals at 11.61 ppm and 10.77 ppm, respectively, in the ^{15}N-HSQC spectra of the two FHA domains (Figure 2B). The neutral $N^{\varepsilon2}H$ tautomeric state of H251 in FHA-2 at pH 6 is unambiguously shown by the highly diagnostic chemical shifts of its deprotonated $N^{\delta1}$ (253 ppm) and protonated $N^{\varepsilon2}$ (170 ppm) imidazole ring nitrogens (Platzer et al., 2014). In the case of H50, this conclusion is derived from a physicochemical consideration of the high-resolution crystal structure of FHA-1, combined with NMR spectral features closely resembling those of FHA-2.

FHA-2 Binds pThr Peptides with Higher Affinity than FHA-1

The interactions of the Rv1747 FHA domains with short phosphopeptides corresponding to the reported PknF acceptor sites pT152 and pT210 in the ID linker were characterized by NMR spectroscopy and ITC. In ^{15}N-HSQC-monitored titrations, both FHA domains bound both phosphopeptides (Figures 4A, S4, and S5). Furthermore, based on the fit K_d values from these titrations (Table 3 and Figure S6), neither FHA domain showed any significant discrimination between the two peptides. This is consistent with the observation that, beyond the invariant pThr, FHA domain specificity is often set by the pT+3 residue (Liang and Van Doren, 2008; Mahajan et al., 2008). In the case of the two peptides (pT^{152}TRI and pT^{219}SMM), these both have long, hydrophobic sidechains. In contrast, the peptides bound the two FHA domains with substantially different, albeit modest, affinities. The K_d values for either pT152 or pT210 phosphopeptide with FHA-1 were in the near mM range, whereas those with FHA-2 were ~20- to 30-fold lower.

The same series of titrations were also measured using the complementary technique of ITC, and comparable K_d values were obtained (Table 3 and Figure S7). Due to the relatively weak interactions of FHA-1 with the phosphopeptides, reliable ΔH values could not be obtained. In the case of FHA-2, binding was accompanied by a favorable enthalpic change offset by an unfavorable net loss of entropy. For consistency, these calorimetric and spectroscopic studies were carried out at pH 6, with this condition chosen to reduce potential loss of NMR signals from amides in disordered regions of the proteins due to HX. Upon raising the sample pH to 8, the pT152 peptide bound both FHA-1 and FHA-2 with moderately higher affinity (Table 3). This may result in part from an increase in the net negative charge of the phosphate group (unperturbed second $pK_a \sim 6.3$ for pThr; Bienkiewicz and Lumb, 1999) and thus enhanced electrostatic interactions with the conserved R33/R234 in the binding clefts of the FHA domains (Figures 3C and 3D). Previously published ITC measurements of the same protein-phosphopeptide combinations at pH 8 revealed larger negative ΔH values with FHA-2 than FHA-1, yet relatively uniform K_d values of ~2 μM (Spivey et al., 2011). The differences in these measured affinities likely arise from differences in exact experimental conditions.

FHA-2 Exhibits Larger NMR Spectral Perturbations than FHA-1 upon Phosphopeptide Binding

The NMR-monitored titration experiments also provide insights into the mechanism of phosphopeptide binding. When mapped onto the structures of FHA-1 and FHA-2, residues showing pronounced amide chemical shift perturbations upon addition of either the pT152 or pT210 peptides cluster near the canonical FHA domain binding interface (Figures 4B–4D). However, a visual comparison of the ^{15}N-HSQC titration spectra presented in Figures 4A, S4, and S5 shows clear differences in the effects of the peptides on the two FHA domains.

In the case of FHA-1, only a relatively small number of amides had perturbed NMR signals and, of those, most exhibited progressive chemical shift changes upon titration with either phosphopeptide. This is diagnostic of binding in the fast exchange limit, whereby the exchange rate constant $k_{ex} = k_{on}[peptide] + k_{off}$ is much greater than the resonance frequency difference $\Delta\omega$ between free and bound states (Kleckner and Foster, 2011). This is also consistent with the relatively weak $K_d = k_{off}/k_{on}$ values for binding. A few amides, including S47 and

Figure 2. The Rv1747 Regulatory Module Is Composed of Independent FHA Domains Joined by an ID Linker

(A) The FHA-1 (Rv1747$^{1-156}$; blue), FHA-2 (Rv1747$^{206-310}$; red) and full regulatory module (Rv1747$^{1-310}$; black) constructs.

(B) The ^{15}N-HSQC spectra of FHA-1 (blue) and FHA-2 (red) overlaid on that of the full regulatory module (black). The near identical $^{1}H^{N}$-^{15}N chemical shifts of corresponding residues indicate that the FHA domains are structurally independent and do not interact when joined to form the regulatory module. Additional ID linker residues have random coil $^{1}H^{N}$ chemical shifts near 8–8.5 ppm. The highly downfield shifted signals from the amides of S47 and S248, as well as the slowly exchanging $^{1}H^{\varepsilon2}$-$^{15}N^{\varepsilon2}$ imidazoles (aliased) of neutral H50 and H251, in the peptide-binding clefts of FHA-1 and FHA-2, respectively, are identified. See Figure S1 for assigned spectra.

(C) Normalized β-strand and α-helix propensities (histograms) and RCI-S^2 values (black lines; decreasing values from 1 to 0 indicate increasing flexibility) determined from mainchain chemical shifts with MICS. See Figure S2 for ^{15}N relaxation measurements. Conserved residues important for binding are identified in yellow, β-strands 1 and 2 of the canonical FHA fold that are present in FHA-1 but absent in FHA-2 are in cyan, and the additional C-terminal β-strand 1* of FHA-2 is in magenta. The β-strands (arrows) from the FHA-1 crystal structure are also indicated.

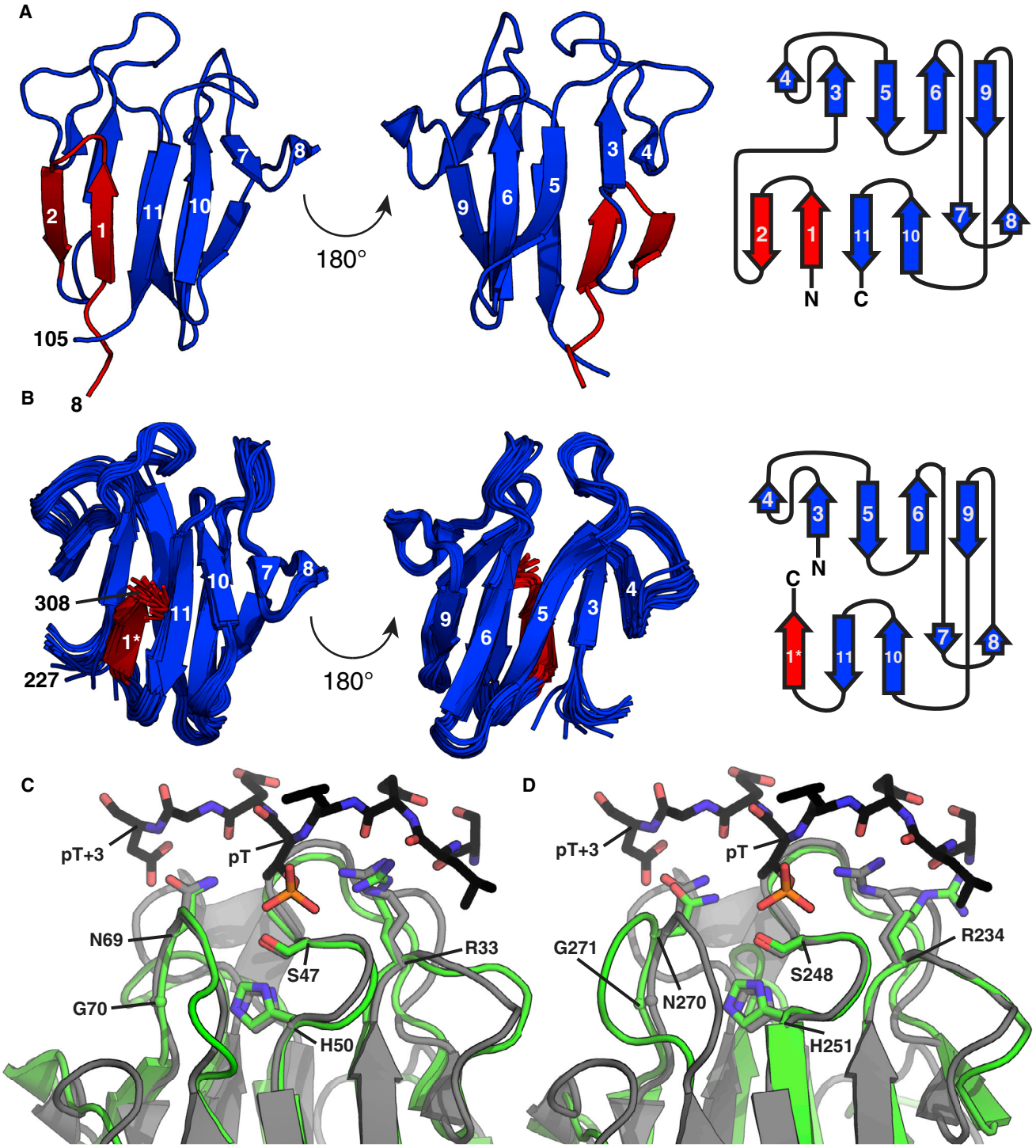

Figure 3. FHA-2 Has a Circularly Permuted FHA Domain Fold with a Conserved pThr-Binding Interface

(A and B) Structure and topology diagrams of (A) FHA-1 ($Rv1747^{3-116}$) determined by X-ray crystallography and (B) FHA-2 ($Rv1747^{206-310}$) determined by NMR spectroscopy. Highlighted in red are the N-terminal β-strands 1 and 2 of FHA-1 and the corresponding C-terminal strand 1* of FHA-2.

(C and D) Overlaid representations of the X-ray crystallographic structure of pThr peptide-bound Rad53 FHA1 domain (PDB: 1G6G, gray) with (C) the crystal structure of unbound FHA-1 (green) and (D) the lowest energy member of the NMR-derived structural ensemble of unbound FHA-2 (green). Important residues in the binding interfaces are shown as sticks (oxygen, red; nitrogen, blue; hydrogens omitted). The Rad53-bound peptide has the carbon and phosphorous atoms of pThr in orange and remaining carbons in black. In all three structures, the central histidine is in its neutral $N^{\varepsilon 2}H$ tautomeric form to accept a hydrogen bond from the amide of the adjacent serine and to donate a hydrogen bond to the carbonyl of a conserved glycine. See Figure S3 for sequence and structure alignments.

Table 1. X-Ray Crystallography Data Collection and Refinement Statistics for FHA-1 ($Rv1747^{3–116}$)

Derivative	Native	NaBr		
Space group	$P3_221$	$P3_221$		
Data Collection				
Unit cell dimensions				
a = b, c (Å)	58.92, 58.92, 68.63	59.05, 59.05, 68.39		
α = β, γ (°)	90, 90, 120	90, 90, 120		
Wavelength (Å)	1.1159	0.920	0.9202	1.1159
Resolution (Å)	68.6–1.8 (1.84–1.8)	50–2.0	50–2.0	50–2.0
Observations	109,053	289,614	289,834	164,976
Unique reflections	11,508	9,723	9,753	9,697
Multiplicity[a]	9.5 (4.9)			
$<I/\sigma I>$[a]	26.0 (1.9)	11 (2.5)	12.4 (1.8)	35.9 (8.2)
Data coverage (%)	87.0 (46.2)	100	100	100
R_{merge}[b]	6.9 (82.2)	15.1 (52.0)	13.8 (67.0)	6.0 (26.0)
Mean figure of merit[c]		0.72 (0.50)		
Refinement Statistics				
Resolution range (Å)	51.0–1.80			
Reflections used	21,394			
Mean B factor ($Å^2$)	24.1			
R_{cryst} (%)[d]	16.9			
R_{free} (%)	20.8			
Root-Mean-Square Deviations[e]				
Bonds (Å)	0.007			
Angles (°)	1.13			
Ramachandran				
Most favored (%)	97.0			
Allowed (%)	3.0			

[a]Parentheses denote values for the highest resolution shell.
[b]$R_{merge} = \Sigma|I - <I>|/\Sigma I$; I, intensity.
[c]Mean figure of merit (after density modification) = $<|\Sigma P(\alpha)e^{i\alpha}/\Sigma P(\alpha)|>$; α, phase; $P(\alpha)$, phase probability distribution.
[d]$R_{cryst} = \Sigma|F_o - F_{calc}|/\Sigma F_o$ with observed (F_o) and calculated (F_{calc}) structure-factor amplitudes.
[e]Root-mean-square deviations from ideal values.

N69, exhibited intermediate exchange broadening ($k_{ex} \sim \Delta\omega$). This can be explained by their intimate involvement in the binding interface and hence a large $\Delta\omega$ accompanying phosphopeptide association. Since only 50%–60% saturation was achieved in the titration experiments with FHA-1, sharpening and reappearance of these signals from the fully bound state was not observed.

In contrast to FHA-1, numerous amides in FHA-2 showed spectral perturbations upon binding either phosphopeptide. In accordance with K_d values in the 10 μM range, amides with larger $\Delta\omega$ values also exhibited line broadening at intermediate titration points (fast-intermediate exchange regime). Somewhat surprisingly, the signals from numerous amides disappeared in the presence of sub-stoichiometric amounts of peptide without the concomitant appearance of new signals from the bound state (90%–95% saturation), as would be expected for slow exchange binding. This is suggestive of conformational exchange broadening in the bound state. Most residues with complete peak attenuation in spectra of FHA-2 were located in or close to the canonical peptide-binding interface, including R234, S248, and N270. It is also noteworthy that the $^1N^H$-^{15}N signals of residues in the appended C-terminal strand 1*, as well as strand 11, in FHA-2 were more perturbed than those in the equivalent strands 1 and 11 of FHA-1. Thus, the circularly permuted region of FHA-2 is also affected by phosphopeptide binding.

Overall, our NMR titrations reveal that pT152 and pT210 phosphopeptide binding leads to significantly more amides showing larger chemical shift perturbations and exchange broadening in FHA-2 compared with FHA-1. This correlates with their relative affinities, and points to a larger binding interface and/or greater conformational perturbations upon association for FHA-2 than FHA-1. Such perturbations could, for example, involve changes in hydrogen bonding, upon which amide chemical shifts are highly sensitive. The bound state of FHA-2 also appears to undergo conformational exchange as indicated by the absence of many amide signals upon saturation. Furthermore, results from ITC experiments indicate that pThr peptide binding by FHA-2 is associated with an entropic loss, which is offset by a large enthalpy change. Taken together, these results suggest that

Table 2. NMR Spectroscopy Data Collection and Refinement Statistics for FHA-2 ($Rv1747^{206–310}$)

NMR Distance and Dihedral Restraints	
Distance restraints	
Total nuclear Overhauser effect	1,302
Intraresidue	347
Sequential ($\|i - j\| = 1$)	360
Medium range ($\|i - j\| < 4$)	135
Long range ($\|i - j\| > 5$)	460
Hydrogen bonds (present in >6 models)	63
Dihedral angle restraints	
Φ	68
Ψ	68
Structure Statistics	
Violations (mean ± SD)	
Distance restraints (Å)	0.005 ± 0.002
Dihedral angle restraints (°)	4.1 ± 0.2
Max. distance restraint violation (Å)	0.54
Max. dihedral angle violation (°)	26
Ramachandran plot (%)	
Most favored	91.0
Additionally allowed	7.6
Generously allowed	0.3
Disallowed	1.0
Average pairwise root-mean-square deviations[a] (Å)	
Backbone atoms	0.48 ± 0.1
Heavy atoms	0.96 ± 0.1

[a]Pairwise root-mean-square deviation calculated among the 20 refined structures for residues 28–104.

the conformational adaptability of FHA-2 allows for a more favorable bound state. The direct correlation of phosphopeptide affinity with flexibility for the FHA domains is bolstered by denaturation and amide HX studies.

FHA-2 Is More Dynamic and Less Stable than FHA-1

To help understand their different structural and phosphopeptide-binding properties, we probed the stability and dynamics of FHA-1 and FHA-2 both experimentally and computationally. In chemical denaturation studies monitored with circular dichroism (CD) spectroscopy, the domains unfolded at distinctly different mid-point $[GuHCl]_{1/2}$ of 1 M (FHA-1) and 0.5 M (FHA-2) (Figures 5A–5C). Non-linear regression of these data yielded values of 3.2 ± 0.3 and 2.3 ± 0.8 kcal/mol for $\Delta G_{u,H_2O}$, the extrapolated free energy change upon unfolding of FHA-1 and FHA-2, respectively, in the absence of denaturant. By both criteria, FHA-2 is substantially less stable than FHA-1.

This conclusion is supported by protection factors (PFs) obtained from amide HX measurements (Figures 5D and 5E). Under EX2 conditions, PFs provide a measure of the residue-specific free energy changes, $\Delta G_{HX} = 2.303RT\log(PF)$, governing local or global conformational equilibria leading to exchange. The most slowly exchanging amides in FHA-1 have PFs ~100-fold greater than those in FHA-2 ($\log(PF)_{max} \sim 5.75$ versus 3.5). Assuming these amides exchange via global unfolding, this corresponds to ΔG_{HX} values of 7.8 kcal/mol and 4.8 kcal/mol for the FHA domains, respectively. Differences between these values and those obtained via chemical denaturation experiments are attributed to the different experimental conditions used for the two approaches and the extrapolations made to extract free energy changes. Nevertheless, the key conclusion is that FHA-1, with a canonical 11-strand FHA domain fold, is more stable than the circularly permuted 10-strand FHA-2.

HX measurements also reveal that circular permutation has an effect on the dynamics of various parts of the FHA domain. Whereas the interacting N- and C-terminal β-strands 1 and 11 are highly protected in FHA-1, the terminal strand 3 and 1* of FHA-2 are not interacting and much less protected. Furthermore, amides in or close to the binding interface of FHA-2, including those of residues following strand 3 and in the loop connecting strands 6 and 7, have lower PFs than the corresponding amides in FHA-1. This finding indicates higher relative flexibility for these regions of FHA-2. Importantly, this aligns well with the segments of FHA-2 that displayed pronounced chemical shift changes upon phosphopeptide binding (Figure 4). The correlation of large peptide-dependent spectral perturbations with low unbound state PFs suggests that FHA-2 has a conformationally dynamic binding interface. In contrast, FHA-1 shows somewhat more uniform PFs, with strands 1 and 2 well protected from HX. The greater stability and lower flexibility of FHA-1 may explain the relatively small spectral perturbations upon phosphopeptide binding.

To further investigate the dynamics of both FHA domains, we conducted 900 ns all-atom MD simulations in explicit water using the AMBER force field. Over the course of the runs, FHA-1 and FHA-2 remained stable with average C^{α} root-mean-square deviations from the corresponding experimental structures of only 0.75 Å and 1.35 Å, respectively (Figures S8A and S8B). AMBER back-calculated B-factors, which report on the magnitude of structure dynamics in the nano- to microsecond timescale, showed that, for both domains, the β-strands were rigid, whereas the connecting hairpins and loops were mobile (Figures S8C–S8F). Most strikingly, for strand 1*, the fluctuations in FHA-2 were clearly larger than in the corresponding regions in FHA-1. This higher mobility in strand 1* might be caused by a lack of a stabilizing strand 2 and corroborates the low PFs measured for this region of FHA-2.

FHA-1 and FHA-2 Bind the Phosphorylated Linker to Form Inter- and Intramolecular Complexes

Both FHA-1 and FHA-2 bind short phosphopeptides corresponding to pT152 and pT210. However, within their native context, the FHA domains and phospho-acceptors lie within the same polypeptide chain. Therefore, we investigated the effects of phosphorylation on two constructs, $Rv1747^{1–213}$ and $Rv1747^{148–310}$, spanning FHA-1 or FHA-2 and the two reported phospho-acceptor threonines in the following or preceding linker region, respectively. The proteins were modified *in vitro* using the catalytic domain of PknF. The addition of two phosphates was confirmed by mass spectrometry. NMR spectral changes (Figure S9), as well as the effects of phospho-ablative alanine substitutions (Figures 6, S10B, and S10C), were consistent with T152 and T210 as the specific sites of modification.

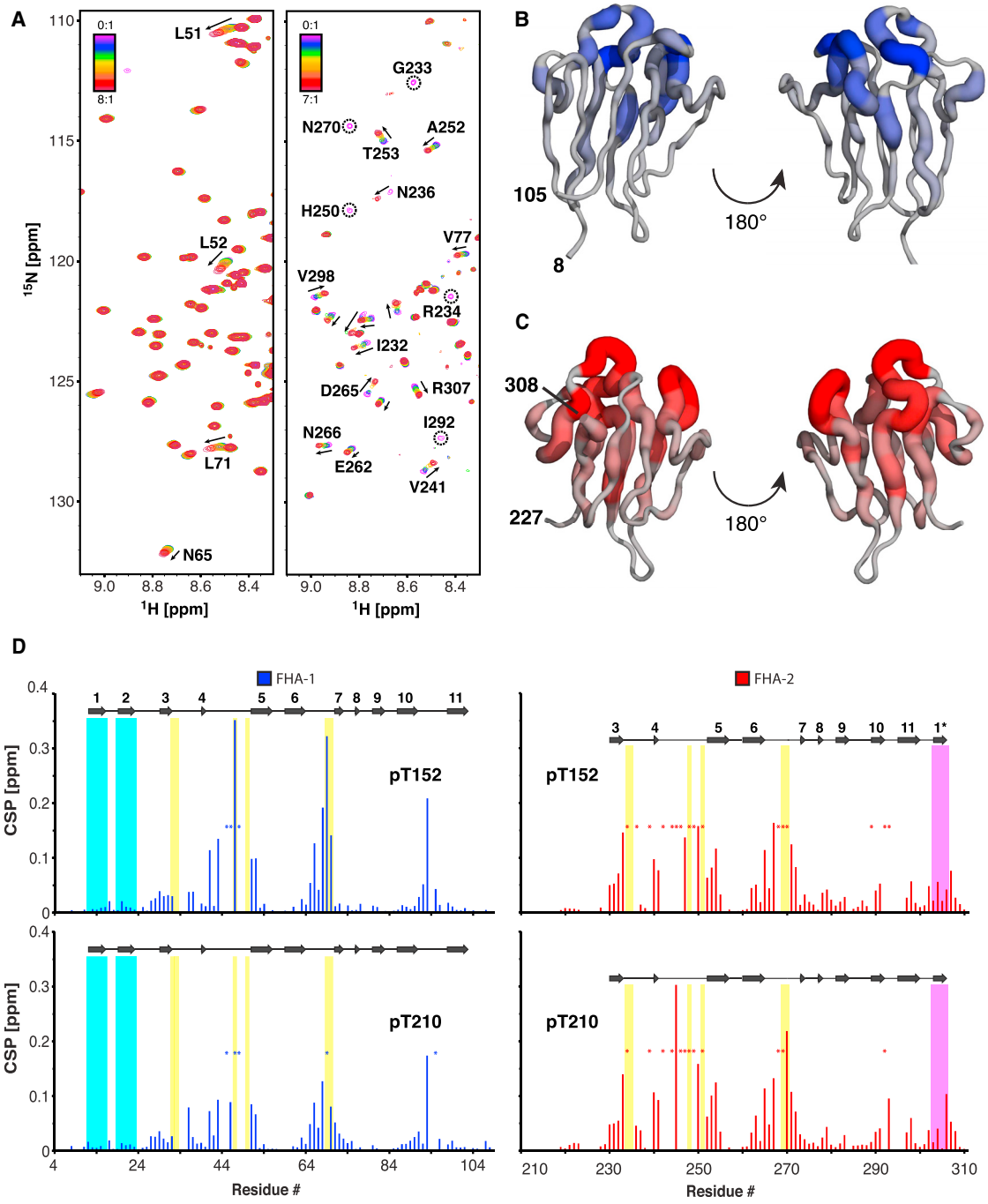

Figure 4. FHA-1 and FHA-2 Bind Phosphothreonine Peptides

(A) Overlaid ^{15}N-HSQC spectra of uniformly ^{15}N-labeled FHA-1 (Rv1747$^{1-156}$; left) and FHA-2 (Rv1747$^{206-310}$; right) titrated with unlabeled pT152 and pT210 phosphopeptides, respectively. Peptide:protein ratios are indicated with rainbow coloring. Progressive shift changes of selected amides undergoing binding in the fast exchange limit are shown by arrows. Amides exhibiting severe intermediate exchange broadening are identified with dashed circles. See Figures S4–S6 for full spectra and fit binding isotherms.

(B) Chemical shift perturbations (CSPs) upon binding the pT152 peptide mapped in a gray-blue color and tube thickness gradient onto the structure of FHA-1. Similar changes occurred with the pT210 peptide.

(C) CSPs upon binding the pT210 peptide mapped in a gray-red color gradient onto the structure of FHA-2. Similar changes occurred with the pT152 peptide.

(D) Amide CSPs upon binding of pT152 (8:1 molar excess, 59% and 94% saturated for FHA-1 and FHA-2, respectively, based on K_d values in Table 3) and pT210 (7:1 molar excess, 52% and 92% saturated for FHA-1 and FHA-2, respectively) peptides by FHA-1 and FHA-2. Asterisks identify exchange broadened amides. Conserved binding residues are highlighted in yellow, β-strands 1 and 2 of FHA-1 in cyan, and the additional C-terminal strand 1* of FHA-2 in magenta. Missing data correspond to prolines and amides with overlapping or unassigned signals.

Table 3. NMR Spectroscopic and ITC Studies of FHA-Phosphopeptide Interactions

Protein Construct	pH	Phospho-peptide	K_d (NMR)[a] (μM)	K_d (ITC)[a] (μM)	ΔH (kcal/mol)	ΔS (cal/mol K)
FHA-1 ($Rv1747^{1-156}$)	6	pT210	750 ± 170	560 ± 40		
	6	pT152	680 ± 110	350 ± 190		
	8	pT152		100 ± 60		
FHA-2 ($Rv1747^{206-310}$)	6	pT210	23 ± 5	23 ± 3	- 11.9 ± 0.5	- 19 ± 2
	6	pT152	38 ± 15	72 ± 12	- 31 ± 2	- 84 ± 7
	8	pT152		32 ± 7	- 12 ± 2	- 20 ± 7

[a]See Figures S6 and S7 for binding isotherms.

First, we carried out ^{15}N-HSQC-monitored titrations of ^{15}N-labeled non-phosphorylated samples of $Rv1747^{1-213}$ (Figures 6A and 6B) and $Rv1747^{148-310}$ (Figures 6D and 6E) with doubly phosphorylated, unlabeled (NMR-silent) versions of the same construct. The chemical shift perturbations of backbone amides observed in these titrations paralleled those with either synthetic peptide. From this, we unambiguously conclude that intermolecular (*trans*) binding occurs with both constructs such that pT152 and/or pT210 on one molecule can bind the FHA domain on another molecule.

To investigate the possibility of intramolecular (*cis*) FHA-pThr binding, we compared the ^{15}N-HSQC spectra of ^{15}N-labeled $Rv1747^{1-213}$ and $Rv1747^{148-310}$ in their unmodified versus doubly phosphorylated forms (Figures 6C, 6F, and S9). *In vitro* phosphorylation of the linker threonines of these constructs (~300 μM) caused amide chemical shift perturbations in their FHA domains that approximately matched those observed at the titration endpoints with the phosphorylated peptides. However, these endpoints, with ~2.4 mM pT152 and ~2.1 mM pT210 phosphopeptide (~300 μM protein), corresponded to ~50%–60% saturation of the FHA-1 construct and 90%–95% of FHA-2 (Figures 6A and 6D). In contrast, the doubly phosphorylated proteins were ~300 μM, and thus 7- or 8-fold more dilute than the phosphopeptides.

The apparent higher net affinity of the FHA domains for phosphorylated linkers (i.e., in the context of the $Rv1747^{1-213}$ and $Rv1747^{148-310}$ constructs) versus short phosphopeptides is attributed to two possible mechanisms that augment the demonstrated intermolecular interactions. The first of these is intramolecular (*cis*) binding in which one of the phosphorylated threonines binds the FHA domain within the same molecule. In the second mechanism, which can be considered as avidity or multivalent cooperativity (Mammen et al., 1998), two or more molecules form a complex via intermolecular interactions and then FHA domains and phosphothreonines within the complex associate. In either case, the intramolecular or intracomplex interactions are entropically favored due to the increased local effective concentrations of the FHA domains and phosphorylated linkers. However, dissecting the contributions of the possible microscopic intra- and intermolecular binding equilibria to the overall macroscopic association of the Rv1747 constructs is not easily accomplished. Although in principle distinguishable through concentration dependent studies, this is limited in practice by the low sensitivity of NMR spectroscopy.

Further insights in the association states of the Rv1747 constructs were gained from their correlation times τ_C for global isotopic rotational diffusion as measured via amide ^{15}N relaxation experiments (Figures 6G and S10A). In their unmodified states, $Rv1747^{1-213}$ (23 kDa) and $Rv1747^{148-310}$ (17 kDa) had correlation times of 9.9 ns and 6.9 ns, respectively. These values are consistent with monomeric species composed of a folded FHA domain and an appended ID linker. Upon dual phosphorylation, these correlation times increased to 13 ns, confirming that the proteins form intermolecular complexes. Although roughly indicative of dimers, it is important to note that these correlation times are averaged over all forms of the constructs present, including monomers with intramolecular FHA-pThr interactions, dimers with each FHA domain binding a partner phosphothreonine, and a variety of possible oligomers. Variants of $Rv1747^{1-213}$ and $Rv1747^{148-310}$ with alanine substitutions at positions 152 or 210 to restrict phosphorylation to a single site in the ID linker were also investigated. Although capable of dimerization, these species gave τ_C values intermediate to those of the unmodified and dual phosphorylated proteins. This further suggests that intramolecular interactions contribute to the FHA-pThr binding observed by NMR spectroscopy, and, in the case of the singly phosphorylated proteins, compete with intermolecular binding. However, with two linker phosphothreonines, both binding modes can occur to yield, on average, dimeric-like complexes. Indeed, it is interesting that $Rv1747^{1-213}$ and $Rv1747^{148-310}$ do not make extended head-to-tail polymers upon double phosphorylation. This also suggests that intramolecular or intracomplex interactions occur, thereby favoring dimeric or limited oligomeric species.

NMR spectral perturbations resulting from the single-site phosphorylation of the T152A and T210A variants provided evidence for differential interactions of the two FHA domains and the two linker phospho-acceptors (Figures S10B and S10C). In the case of the $Rv1747^{1-213}$ constructs, phosphorylation at pT152 yielded only small chemical shift changes of diagnostic amides relative to the unmodified protein, whereas phosphorylation at pT210 caused changes resembling those resulting from double phosphorylation of the wild-type protein. In the case of the $Rv1747^{148-310}$ constructs, pT152 yielded intermediate chemical shift changes between the unmodified and fully phosphorylated endpoints, whereas pT210 also caused spectral perturbations resembling those resulting from double phosphorylation. These spectral changes are difficult to interpret in detail due to *cis* and *trans* binding modes and an order-of-magnitude difference in phosphothreonine peptide-binding affinity exhibited by FHA-1 versus FHA-2. Nevertheless, the data point to differences in the accessibility, or local concentration, of the

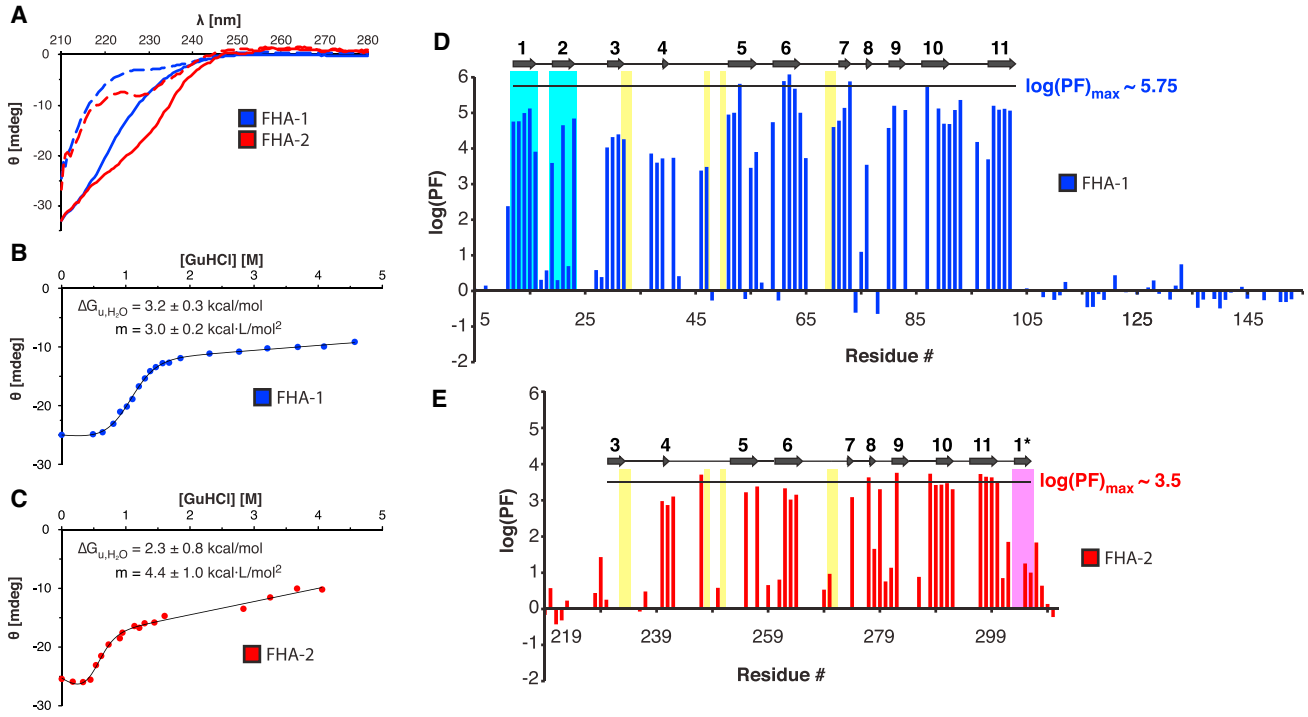

Figure 5. FHA-1 Is More Stable and Less Dynamic than FHA-2

(A) CD spectra of FHA-1 (Rv1747$^{1-156}$; blue) and FHA-2 (Rv1747$^{206-310}$; red) in their folded (solid lines, 0 M GuHCl) and unfolded (dashed, 5 M GuHCl) states. (B and C) CD signals for (B) FHA-1 (blue, 217 nm) and (C) FHA-2 (red, 217.5 nm) as a function of GuHCl concentration at 25°C. The data were fit to obtain the indicated $\Delta G_{u,H_2O}$ values for the unfolding of FHA-1 and FHA-2, respectively, in the absence of denaturant.

(D and E) Histograms of combined amide $^1H/^2H$ (pH* 6) and $^1H/^1H$ (pH 6–8) exchange PFs measured for (D) FHA-1 and (E) FHA-2 at 25°C. The horizontal lines indicate the largest PFs for each domain, attributed to slowest exchange via global unfolding. In contrast, the disordered linker residues have PFs ~1. Conserved binding residues are highlighted in yellow. β-strands 1 and 2 present in only FHA-1 and the additional C-terminal strand 1* in FHA-2 are in light cyan and magenta, respectively. Missing data correspond to prolines, amides with overlapping or unassigned signals, or amides for which reliable slow ($^1H/^2H$) or fast ($^1H/^1H$) exchange rate constants could not be obtained over the conditions examined.

phosphothreonines in the ID linker with respect to the flanking FHA domains.

Phosphorylated Regulatory Module Forms Higher Order Complexes

We also studied the effect of phosphorylation on the full FHA regulatory module (Rv1747$^{1-310}$), which contains in one polypeptide chain both FHA-1 and FHA-2 as well as the ID linker with two phospho-acceptor threonines (Figure 7). Two hours after addition of PknF directly to the ^{15}N-labeled protein in an NMR tube, we observed a significant decrease in the intensities of $^1H^N$-^{15}N signals from amides within the structured FHA domains, and to a lesser extent, from the ID linker. Also, NMR signals diagnostic of pThr-bound FHA domains did not appear. After longer incubation times, the sample became visibly turbid and only signals from the ID linker were detected (not shown). A simple interpretation of these results is that multivalent interactions between the two FHA domains and two phosphorylated threonines within the intervening linker leads to the formation of high molecular mass complexes. In these complexes, the FHA domains are effectively invisible due to rapid relaxation, whereas at least portions of the ID linker are sufficiently flexible to still be detected in ^{15}N-HSQC spectra.

DISCUSSION

Beads-on-a-String Regulatory Module

We have characterized in detail the postulated regulatory module of the *Mtb* ABC transporter Rv1747. This module is composed of two independent FHA domain beads connected by an ID linker string. In contrast to the well-ordered domains, the unmodified linker is conformationally disordered as judged by chemical shift, ^{15}N relaxation, and amide HX measurements. The structure of FHA-1, determined by X-ray crystallography, closely matches that of a canonical FHA domain with 6- and 5-stranded β-sheets forming a β-sandwich. Unexpectedly, the NMR-derived structural ensemble of FHA-2 revealed that this domain is circularly permuted such that a C-terminal strand 1* occupies the standard position of the first N-terminal strand 1. Also, the equivalent of strand 2 is absent. Although it is difficult to infer stability from structure, we speculate that the lower free energy of unfolding for FHA-2 relative to FHA-1, as measured globally by GuHCl denaturation ($\Delta G_{u,H_2O}$) and locally by HX studies (ΔG_{HX}), results from its altered secondary structure. Despite these differences, the two domains share similar global folds and peptide-binding interfaces, including a conserved hydrogen bond network involving a buried, neutral histidine. Thus the functional significance underlying the circular

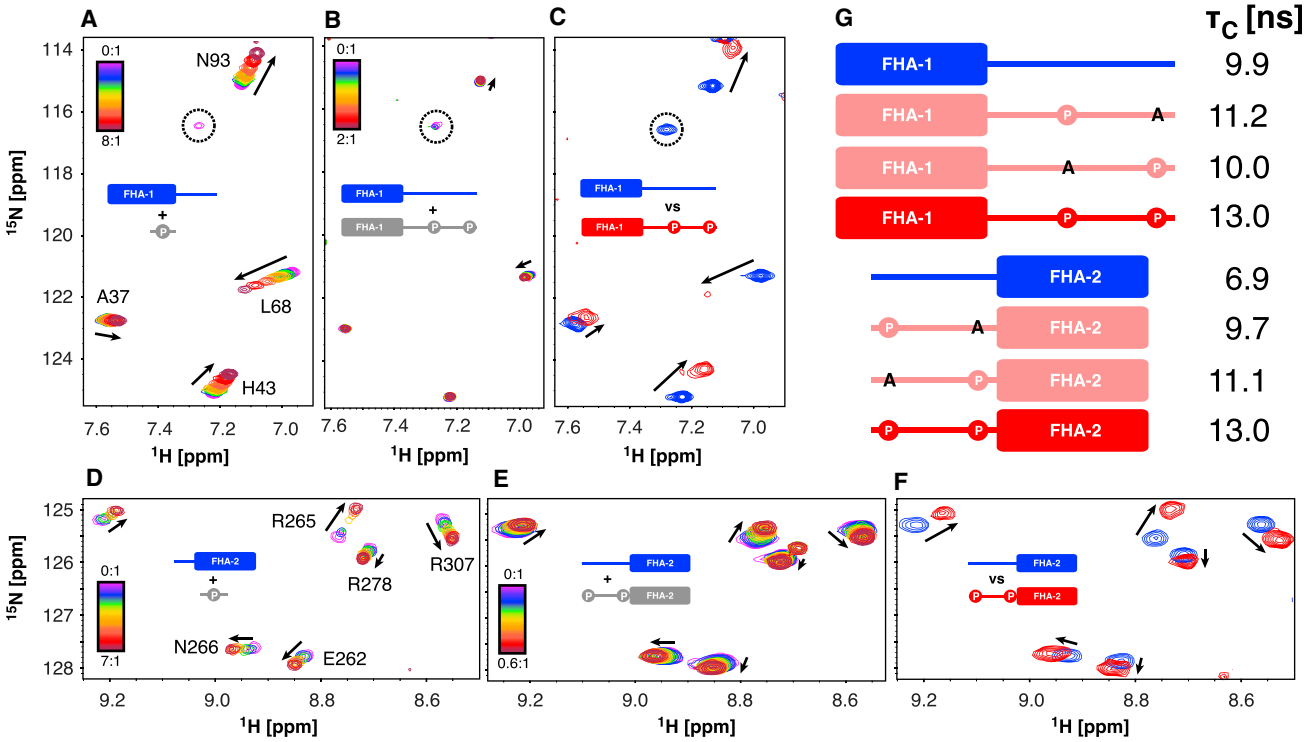

Figure 6. FHA-pThr Mediated Intermolecular Interactions and Oligomerization

(A-C) Overlaid ^{15}N-HSQC spectra for the titration of (A) ^{15}N-labeled FHA-1 (Rv1747$^{1-156}$) with unlabeled pT152 peptide (similar changes occurred with the pT210 peptide) and (B) ^{15}N-labeled FHA-1 (Rv1747$^{1-213}$) with unlabeled FHA-1 (Rv1747$^{1-213}$) phosphorylated at T152 and T210. (C) Overlaid ^{15}N-HSQC spectra of ^{15}N-labeled FHA-1 (Rv1747$^{1-213}$) in its unmodified (blue) and PknF-phosphorylated (red) forms.

(D–F) Overlaid ^{15}N-HSQC spectra for the titration of (D) ^{15}N-labeled FHA-2 (Rv1747$^{206-310}$) with unlabeled pT210 peptide (similar changes occurred with the pT152 peptide) and (E) ^{15}N-labeled FHA-2 (Rv1747$^{148-310}$) with unlabeled FHA-2 (Rv1747$^{148-310}$) phosphorylated at T152 and T210. (F) Overlaid ^{15}N-HSQC spectra of ^{15}N-labeled FHA-2 (Rv1747$^{148-310}$) in its unmodified (blue) and PknF-phosphorylated (red) forms. For comparison, (A) and (D) are reproduced from Figure 4A. In the titrations series, which detect intermolecular binding equilibria, rainbow coloring shows the molar ratios of phosphorylated unlabeled (NMR-silent) to unmodified labeled (NMR-observed) species, arrows highlight amide peaks that shift in fast exchange, and dashed circles identify exchange broadened signals. The smaller CSPs seen upon titration with the phosphorylated proteins versus the phosphopeptides reflect the lower final molar ratios for the former titrations, combined with unobserved intramolecular binding equilibria that compete with the observed intermolecular binding. This is particularly evident for FHA-1, which has higher K_d values for the phosphopeptides than FHA-2. In (C) and (F), the arrows identify peaks that shift upon phosphorylation-mediated intra- and intermolecular association (see Figure S9 for full spectra).

(G) Cartoon representations of the FHA-1 (Rv1747$^{1-213}$) and FHA-2 (Rv1747$^{148-310}$) constructs and their corresponding rotational diffusion correlation times τ_C (Figure S10). All proteins were ~300 μM. Phosphorylated threonines are shown as a circled P, threonine to alanine mutations by an A, and unlabeled species in light gray.

permutation of FHA-2 is unknown. A consequence of shifting the N-terminus of FHA-2 is that the phospho-acceptor T210 lies within the ID linker, and not in β-strand 2, and thus is accessible for modification and binding. However, from an evolutionary perspective, moving the position of the phospho-acceptor within a nonconserved ID linker seems simpler than permuting the conserved β-strand topology of an FHA domain.

The More Dynamic FHA-2 Has Higher Affinity for Phosphopeptides

The affinities of the isolated Rv1747 FHA domains for short phosphopeptide models of the mapped acceptor sites, pT152 and pT210, were measured by NMR spectroscopy and ITC. Both FHA domains bound both peptides with little discrimination. This is consistent with the similarity of the peptides at the pT and pT+3 positions, which serve as key contact points to canonical FHA domains. However, FHA-2 bound the two peptides with 20- to 30-fold higher affinity than FHA-1. The reason for this modest difference (~2 kcal/mol in free energy) is not obvious since the two domains have similar residues within their binding interfaces.

More striking than the differences in K_d values are the differences observed in NMR-monitored titrations. In the case of FHA-1, a relatively small number of amides showed chemical shift perturbations in the fast exchange limit. These amides mapped closely to the expected peptide-binding interface. Although the structure of an FHA-1/peptide complex was not determined, this spectroscopic behavior suggests that FHA-1 has a well-defined interface that undergoes little conformational change upon binding. In contrast, numerous amides mapping to a more extensive interface in FHA-2 exhibited chemical shift changes and/or exchange broadening upon addition of the phosphopeptides. Although attributable to a complex interplay of K_d, k_{on}, k_{off}, and $\Delta\omega$ values, this indicates that peptide binding

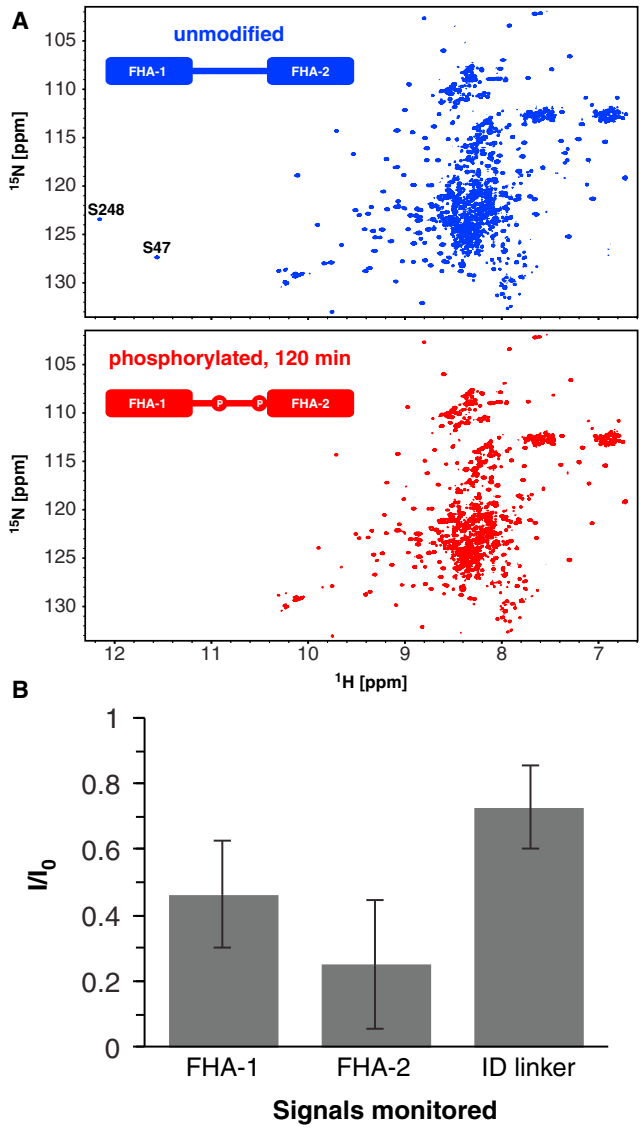

Figure 7. Phosphorylation of the Regulatory Module Leads to Higher Order Association

(A) ^{15}N-HSQC spectra of the unmodified (top, blue) and phosphorylated regulatory module (bottom, red) spanning both FHA domains and the ID linker (Rv1747$^{1-310}$). The unmodified protein was 200 μM in 20 mM sodium phosphate (pH 6.0), 100 mM NaCl, 5 mM $MgCl_2$, and 5 mM ATP. The spectrum of the phosphorylated protein was recorded starting 120 min after addition of 2 μM PknF. Electrospray ionization mass spectrometry confirmed double phosphorylation of Rv1747$^{1-310}$.

(B) Average intensity ratios and standard deviations of corresponding $^{1}H^{N}$-^{15}N signals from assigned residues in FHA-1 and FHA-2 before (I_0) and after phosphorylation (I). Signal loss indicates oligomerization to higher molecular mass species due to intermolecular FHA-pThr interactions. Unassigned amides from the more mobile ID linker showed less intensity perturbations.

causes more extensive conformational changes in FHA-2 than in FHA-1. Furthermore, even at near saturation, signals from several FHA-2 amides did not appear, implying that milli- to microsecond timescale conformational exchange still occurs within the bound state. Without high-resolution models of the bound complexes, the magnitudes of these changes are difficult to estimate, yet are likely on the Angstrom scale given the similarities of the unbound FHA-1 and FHA-2 structures.

Combining these results, we hypothesize that the higher affinity of FHA-2 versus FHA-1 for phosphopeptides is linked to its lower stability and greater conformational dynamics. These dynamic properties are seen in particular through HX studies, with FHA-2 having low residue-specific PFs, as well as through MD simulations. The correlation of dynamics and ligand affinity suggests that the conformational plasticity of FHA-2 enables a more favorable bound state with phosphothreonine motifs in the Rv1747 linker. Although FHA domains have been considered to be relatively rigid pThr-binding modules, there are cases in which dynamics play an important role in ligand recognition (Liang and Van Doren, 2008; Mahajan et al., 2008). The circularly permuted FHA-2 is a striking example of the latter.

FHA Domains Bind Phosphorylated Linker Threonines via Inter- and Intramolecular Equilibria

Using NMR spectroscopy, we demonstrated that fragments of Rv1747 spanning one or both FHA domains and the intervening linker exhibit intermolecular (*trans*) and intramolecular (*cis*) modes of FHA-pThr association. Unfortunately, it was not possible to quantitatively dissect the contributions of a myriad of possible microscopic binding equilibria toward these processes. Qualitatively, phospho-ablative T152A and T210A variants with single phosphothreonines had correlation times τ_C for rotational diffusion intermediate to those of the monomeric unmodified proteins and the (on average) dimer-like doubly phosphorylated species. Such diminished intermolecular association is expected because the overall concentration of phosphothreonines in the monophosphorylated proteins is effectively reduced relative to the doubly modified proteins. The position of the phosphothreonine (pT152 or pT210) in the linker relative to FHA-1 and FHA-2 also influenced the measured τ_C values and resulted in different patterns of diagnostic ^{15}N-HSQC spectral perturbations. This stands in contrast to the approximately equal affinity of peptide models of the pT152 and pT210 sites for each FHA domain. Collectively, these results indicate that, when connected within a polypeptide chain, the two phosphothreonines have different accessibilities or local concentrations for binding FHA-1 versus FHA-2 to form intra- and intermolecular complexes. This may enable tunable regulation Rv1747 through a gradation of phosphorylation-dependent self-association equilibria.

Potential Mechanisms for Regulating Rv1747 Transporter Function

The exact biochemical functions of Rv1747 remain to be established. However, growing evidence convincingly implicates this protein in the transport of *Mtb* cell wall precursors. A distinguishing feature of Rv1747 is its appended N-terminal regulatory module with phospho-acceptor sites for the *Mtb* STPK PknF. Evidence for the phosphorylation-dependent regulatory role of this module follows from the reduced infectivity of *Mtb* strains harboring Rv1747 variants with phosphor-ablative T152A/T210A mutations in the linker region or mutations in the binding cleft of FHA-1 (Spivey et al., 2011).

According to the canonical ABC transporter architecture, the expected active quaternary state of Rv1747 is that of at least a

homodimer. We thus propose that intermolecular pThr-FHA binding between regulatory modules either favors the assembly of Rv1747 into functional dimers or higher order oligomers, or alters intracomplex interactions (e.g., of the NBDs) to impact the activity of existing dimers/oligomers. With two FHA domains and at least two phospho-acceptor threonines showing differential levels of intra- and intermolecular binding, either general mechanism could lead to graded, rather than all-or-none, regulation of Rv1747. This is in line with previous studies showing that proteins containing both an FHA domain and phospho-acceptor threonines can self-associate upon phosphorylation (Weng et al., 2015) or exhibit intramolecular binding to autoinhibit heterotypic partnerships (Barthe et al., 2009; Nott et al., 2009). Indeed, FHA domains were found to be enriched in proteins containing sequences predicted to be autoinhibitory (Yeon et al., 2016). Ascertaining the functionally relevant oligomerization states of Rv1747 in *Mtb* cells will require detailed *in vivo* studies using approaches such as super-resolution light microscopy.

Complete phosphorylation of T152 and T210 is seen when the isolated regulatory module is treated with the catalytic domain of PknF *in vitro*. However, other *Mtb* STPKs have been reported to phosphorylate Rv1747 (Grundner et al., 2005) and additional phosphorylation sites have been identified by proteomics studies (Fortuin et al., 2015). Thus *in vivo*, the phosphorylation levels of Rv1747 are likely dependent on the concentrations and activities of several kinases, which in turn are susceptible to environmental stimuli, as well as on PstP, the sole *Mtb* serine/threonine protein phosphatase. Further layers of control could also arise, for example, via FHA domain recruitment of pThr-modified STPKs (Villarino et al., 2005) or phosphoproteins such as the recently identified stress factor Rv2623 (Glass et al., 2017). Collectively, this would lead to a sophisticated regulatory system for Rv1747 that could be tuned on multiple levels to enable the growth and survival of *Mtb* within host macrophages.

STAR★METHODS

Detailed methods are provided in the online version of this paper and include the following:

SUPPLEMENTAL INFORMATION

Supplemental Information includes ten figures and can be found with this article online at https://doi.org/10.1016/j.str.2018.04.018.

ACKNOWLEDGMENTS

We thank James Fraser and James Holton for assistance with X-ray crystallography. This study was funded by the Canadian Institutes of Health Research (MOP-106622 to Y.A.-G., MOP-136834 to L.P.M.), the Natural Sciences and Engineering Research Council of Canada (J.G.), and the Michael Smith Foundation for Health Research (J.G.). Instrument support was provided by the Natural Sciences and Engineering Research Council of Canada, the Canada Foundation for Innovation, the British Columbia Knowledge Development Fund, and the University of British Columbia.

AUTHOR CONTRIBUTIONS

F.H., J.G., and L.P.M. designed the project and wrote the manuscript. F.H. carried out the experiments, assisted by L.S. for ITC, M.O. with NMR spectroscopy, M.R.-G. and Y.A.-G. with PknF phosphorylation, and J.M.B. with MD simulations. Under the supervision of T.A., L.M.G. solved the X-ray crystal structure of FHA-1, which was subsequently refined by C.L.G.

DECLARATION OF INTERESTS

The authors declare no conflicts of interests.

Received: February 9, 2018
Revised: April 13, 2018
Accepted: April 27, 2018
Published: May 31, 2018

REFERENCES

Adams, P.D., Afonine, P.V., Bunkoczi, G., Chen, V.B., Davis, I.W., Echols, N., Headd, J.J., Hung, L.W., Kapral, G.J., Grosse-Kunstleve, R.W., et al. (2010). PHENIX: a comprehensive Python-based system for macromolecular structure solution. Acta Crystallogr. D Biol. Crystallogr. *66*, 213–221.

Barthe, P., Roumestand, C., Canova, M.J., Kremer, L., Hurard, C., Molle, V., and Cohen-Gonsaud, M. (2009). Dynamic and structural characterization of a bacterial FHA protein reveals a new autoinhibition mechanism. Structure *17*, 568–578.

Bernstein, N.K., Williams, R.S., Rakovszky, M.L., Cui, D., Green, R., Karimi-Busheri, F., Mani, R.S., Galicia, S., Koch, C.A., Cass, C.E., et al. (2005). The molecular architecture of the mammalian DNA repair enzyme, polynucleotide kinase. Mol. Cell *17*, 657–670.

Bienkiewicz, E.A., and Lumb, K.J. (1999). Random-coil chemical shifts of phosphorylated amino acids. J. Biomol. NMR *15*, 203–206.

Braibant, M., Gilot, P., and Content, J. (2000). The ATP binding cassette (ABC) transport systems of *Mycobacterium tuberculosis*. FEMS Microbiol. Rev. *24*, 449–467.

Byeon, I.J., Yongkiettrakul, S., and Tsai, M.D. (2001). Solution structure of the yeast Rad53 FHA2 complexed with a phosphothreonine peptide pTXXL: comparison with the structures of FHA2-pYXL and FHA1-pTXXD complexes. J. Mol. Biol. *314*, 577–588.

Chao, J., Wong, D., Zheng, X., Poirier, V., Bach, H., Hmama, Z., and Av-Gay, Y. (2010). Protein kinase and phosphatase signaling in *Mycobacterium tuberculosis* physiology and pathogenesis. Biochim. Biophys. Acta *1804*, 620–627.

Curry, J.M., Whalan, R., Hunt, D.M., Gohil, K., Strom, M., Rickman, L., Colston, M.J., Smerdon, S.J., and Buxton, R.S. (2005). An ABC transporter containing a forkhead-associated domain interacts with a serine-threonine protein kinase and is required for growth of *Mycobacterium tuberculosis* in mice. Infect. Immun. *73*, 4471–4477.

Case, D.A., Babin, V., Berryman, J.T., Betz, R.M., Cai, Q., Cerutti, D.S., Cheatham, T.E., III, Darden, T.A., Duke, R.E., Gohlke, H., et al. (2014). AMBER 14 (University of California, San Francisco).

Delaglio, F., Grzesiek, S., Vuister, G.W., Zhu, G., Pfeifer, J., and Bax, A. (1995). NMRPipe: a multidimensional spectral processing system based on UNIX pipes. J. Biomol. NMR *6*, 277–293.

Dosset, P., Hus, J.C., Blackledge, M., and Marion, D. (2000). Efficient analysis of macromolecular rotational diffusion from heteronuclear relaxation data. J. Biomol. NMR *16*, 23–28.

Durocher, D., Taylor, I.A., Sarbassova, D., Haire, L.F., Westcott, S.L., Jackson, S.P., Smerdon, S.J., and Yaffe, M.B. (2000). The molecular basis of FHA domain:phosphopeptide binding specificity and implications for phospho-dependent signaling mechanisms. Mol. Cell *6*, 1169–1182.

Emsley, P., Lohkamp, B., Scott, W.G., and Cowtan, K. (2010). Features and development of Coot. Acta Crystallogr. D Biol. Crystallogr. *66*, 486–501.

Fortuin, S., Tomazella, G.G., Nagaraj, N., Sampson, S.L., Gey van Pittius, N.C., Soares, N.C., Wiker, H.G., de Souza, G.A., and Warren, R.M. (2015). Phosphoproteomics analysis of a clinical *Mycobacterium tuberculosis* Beijing isolate: expanding the mycobacterial phosphoproteome catalog. Front. Microbiol. *6*, 6.

Gasteiger, E., Hoogland, C., Gattiker, A., Duvaud, S., Wilkins, M.R., Appel, R.D., and Bairoch, A. (2005). Protein identification and analysis tools on the ExPASy server. In The Proteomics Protocols Handbook, J.M. Walker, ed. (Humana Press), pp. 571–607.

Glass, L.N., Swapna, G., Chavadi, S.S., Tufariello, J.M., Mi, K., Drumm, J.E., Lam, T.T., Zhu, G., Zhan, C., Vilcheze, C., et al. (2017). *Mycobacterium tuberculosis* universal stress protein Rv2623 interacts with the putative ATP binding cassette (ABC) transporter Rv1747 to regulate mycobacterial growth. PLoS Pathog. *13*, e1006515.

Grundner, C., Gay, L.M., and Alber, T. (2005). *Mycobacterium tuberculosis* serine/threonine kinases PknB, PknD, PknE, and PknF phosphorylate multiple FHA domains. Protein Sci. *14*, 1918–1921.

Guntert, P., and Buchner, L. (2015). Combined automated NOE assignment and structure calculation with CYANA. J. Biomol. NMR *62*, 453–471.

Huen, M.S., Grant, R., Manke, I., Minn, K., Yu, X., Yaffe, M.B., and Chen, J. (2007). RNF8 transduces the DNA-damage signal via histone ubiquitylation and checkpoint protein assembly. Cell *131*, 901–914.

Hwang, T.L., van Zijl, P.C., and Mori, S. (1998). Accurate quantitation of water-amide proton exchange rates using the phase-modulated CLEAN chemical EXchange (CLEANEX-PM) approach with a Fast-HSQC (FHSQC) detection scheme. J. Biomol. NMR *11*, 221–226.

Kleckner, I.R., and Foster, M.P. (2011). An introduction to NMR-based approaches for measuring protein dynamics. Biochim. Biophys. Acta *1814*, 942–968.

Krishna, M.M.G., Hoang, L., Lin, Y., and Englander, S.W. (2004). Hydrogen exchange methods to study protein folding. Methods *34*, 51–64.

Langer, G., Cohen, S.X., Lamzin, V.S., and Perrakis, A. (2008). Automated macromolecular model building for X-ray crystallography using ARP/wARP version 7. Nat. Protoc. *3*, 1171–1179.

Lee, H., Yuan, C., Hammet, A., Mahajan, A., Chen, E.S., Wu, M.R., Su, M.I., Heierhorst, J., and Tsai, M.D. (2008). Diphosphothreonine-specific interaction between an SQ/TQ cluster and an FHA domain in the Rad53-Dun1 kinase cascade. Mol. Cell *30*, 767–778.

Lee, W., Tonelli, M., and Markley, J.L. (2015). NMRFAM-SPARKY: enhanced software for biomolecular NMR spectroscopy. Bioinformatics *31*, 1325–1327.

Li, H., Byeon, I.J., Ju, Y., and Tsai, M.D. (2004). Structure of human Ki67 FHA domain and its binding to a phosphoprotein fragment from hNIFK reveal unique recognition sites and new views to the structural basis of FHA domain functions. J. Mol. Biol. *335*, 371–381.

Li, J., Williams, B.L., Haire, L.F., Goldberg, M., Wilker, E., Durocher, D., Yaffe, M.B., Jackson, S.P., and Smerdon, S.J. (2002). Structural and functional versatility of the FHA domain in DNA-damage signaling by the tumor suppressor kinase Chk2. Mol. Cell *9*, 1045–1054.

Liang, X., and Van Doren, S.R. (2008). Mechanistic insights into phosphoprotein-binding FHA domains. Acc. Chem. Res. *41*, 991–999.

Mahajan, A., Yuan, C., Lee, H., Chen, E.S., Wu, P.Y., and Tsai, M.D. (2008). Structure and function of the phosphothreonine-specific FHA domain. Sci. Signal. *1*, re12.

Mammen, M., Choi, S.K., and Whitesides, G.M. (1998). Polyvalent interactions in biological systems: implications for design and use of multivalent ligands and inhibitors. Angew. Chem. Int. Ed. *37*, 2755–2794.

McCoy, A.J., Grosse-Kunstleve, R.W., Adams, P.D., Winn, M.D., Storoni, L.C., and Read, R.J. (2007). Phaser crystallographic software. J. Appl. Crystallogr. *40*, 658–674.

Molle, V., Soulat, D., Jault, J.M., Grangeasse, C., Cozzone, A.J., and Prost, J.F. (2004). Two FHA domains on an ABC transporter, Rv1747, mediate its phosphorylation by PknF, a Ser/Thr protein kinase from *Mycobacterium tuberculosis*. FEMS Microbiol. Lett. *234*, 215–223.

Nott, T.J., Kelly, G., Stach, L., Li, J., Westcott, S., Patel, D., Hunt, D.M., Howell, S., Buxton, R.S., O'Hare, H.M., et al. (2009). An intramolecular switch regulates phosphoindependent FHA domain interactions in *Mycobacterium tuberculosis*. Sci. Signal. *2*, ra12.

Olsson, M.H., Sondergaard, C.R., Rostkowski, M., and Jensen, J.H. (2011). PROPKA3: consistent treatment of internal and surface residues in empirical pKa predictions. J. Chem. Theory Comput. *7*, 525–537.

Otwinowski, Z., and Minor, W. (1997). Processing of X-ray diffraction data collected in oscillation mode. Methods Enzymol. *276*, 307–326.

Pace, N.C., Shirley, B.A., and Thomson, J.A. (1989). Measuring the conformational stability of a protein. In Protein Structure: A Practical Approach, T.E. Creignton, ed. (Oxford University Press), pp. 311–330.

Pallen, M., Chaudhuri, R., and Khan, A. (2002). Bacterial FHA domains: neglected players in the phospho-threonine signalling game? Trends Microbiol. *10*, 556–563.

Platzer, G., Okon, M., and McIntosh, L.P. (2014). pH-dependent random coil ^{1}H, ^{13}C, and ^{15}N chemical shifts of the ionizable amino acids: a guide for protein pK a measurements. J. Biomol. NMR *60*, 109–129.

Roumestand, C., Leiba, J., Galophe, N., Margeat, E., Padilla, A., Bessin, Y., Barthe, P., Molle, V., and Cohen-Gonsaud, M. (2011). Structural insight into the *Mycobacterium tuberculosis* Rv0020c protein and its interaction with the PknB kinase. Structure *19*, 1525–1534.

Ryu, H., Lim, G., Sung, B.H., and Lee, J. (2016). NMRe: a web server for NMR protein structure refinement with high-quality structure validation scores. Bioinformatics *32*, 611–613.

Sattler, M., Schleucher, J., and Griesinger, C. (1999). Heteronuclear multidimensional NMR experiments for the structure determination of proteins in solution employing pulsed field gradients. Prog. Nucl. Magn. Reson. Spectrosc. *34*, 93–158.

Schneider, T.R., and Sheldrick, G.M. (2002). Substructure solution with SHELXD. Acta Crystallogr. D Biol. Crystallogr. *58*, 1772–1779.

Schubert, M., Labudde, D., Oschkinat, H., and Schmieder, P. (2002). A software tool for the prediction of Xaa-Pro peptide bond conformations in proteins based on ^{13}C chemical shift statistics. J. Biomol. NMR *24*, 149–154.

Shen, Y., and Bax, A. (2012). Identification of helix capping and β-turn motifs from NMR chemical shifts. J. Biomol. NMR *52*, 211–232.

Shindyalov, I.N., and Bourne, P.E. (1998). Protein structure alignment by incremental combinatorial extension (CE) of the optimal path. Protein Eng. *11*, 739–747.

Skubak, P., Murshudov, G.N., and Pannu, N.S. (2004). Direct incorporation of experimental phase information in model refinement. Acta Crystallogr. D Biol. Crystallogr. *60*, 2196–2201.

Spivey, V.L., Molle, V., Whalan, R.H., Rodgers, A., Leiba, J., Stach, L., Walker, K.B., Smerdon, S.J., and Buxton, R.S. (2011). Forkhead-associated (FHA) domain containing ABC transporter Rv1747 is positively regulated by Ser/Thr phosphorylation in *Mycobacterium tuberculosis*. J. Biol. Chem. *286*, 26198–26209.

Spivey, V.L., Whalan, R.H., Hirst, E.M., Smerdon, S.J., and Buxton, R.S. (2013). An attenuated mutant of the Rv1747 ATP-binding cassette transporter of *Mycobacterium tuberculosis* and a mutant of its cognate kinase, PknF, show increased expression of the efflux pump-related iniBAC operon. FEMS Microbiol. Lett. *347*, 107–115.

Studier, F.W. (2005). Protein production by auto-induction in high density shaking cultures. Protein Expr. Purif. *41*, 207–234.

Terwilliger, T.C. (2001). Maximum-likelihood density modification using pattern recognition of structural motifs. Acta Crystallogr. D Biol. Crystallogr. *57*, 1755–1762.

Villarino, A., Duran, R., Wehenkel, A., Fernandez, P., England, P., Brodin, P., Cole, S.T., Zimny-Arndt, U., Jungblut, P.R., Cervenansky, C., et al. (2005). Proteomic identification of *M. tuberculosis* protein kinase substrates: PknB recruits GarA, a FHA domain-containing protein, through activation loop-mediated interactions. J. Mol. Biol. *350*, 953–963.

Weng, J.H., Hsieh, Y.C., Huang, C.C., Wei, T.Y., Lim, L.H., Chen, Y.H., Ho, M.R., Wang, I., Huang, K.F., Chen, C.J., et al. (2015). Uncovering the mechanism of forkhead-associated domain-mediated TIFA oligomerization that plays a central role in immune responses. Biochemistry *54*, 6219–6229.

Wu, F.L., Liu, Y., Jiang, H.W., Luan, Y.Z., Zhang, H.N., He, X., Xu, Z.W., Hou, J.L., Ji, L.Y., Xie, Z., et al. (2017). The Ser/Thr Protein kinase protein-protein interaction map of *M. tuberculosis*. Mol. Cell. Proteomics *16*, 1491–1506.

Yeon, J.H., Heinkel, F., Sung, M., Na, D., and Gsponer, J. (2016). Systems-wide identification of cis-regulatory elements in proteins. Cell Syst. *2*, 89–100.

Zhang, Y.Z. (1995). Protein and Peptide Structure and Interactions Studied by Hydrogen Exchange and NMR, PhD Thesis (University of Pennsylvania).

STAR★METHODS

KEY RESOURCE TABLE

REAGENT or RESOURCE	SOURCE	IDENTIFIER
Bacterial and Virus Strains		
E.coli Rosetta 2(λDE3) Singles Competent Cells	Novagen	Cat#71099
E.coli BL21(λDE3) Codon Plus RP Competent Cells	Stratagene	Cat#230250
Chemicals, Peptides, and Recombinant Proteins		
Synthetic peptide pT152: Ac-KKYAGQQLPPA**pT**TRIPAA-NH_2	Biomatik	N/A
Synthetic peptide pT210: Ac-KKYAGTEAGNLA**pT**SMMK-NH_2	Biomatik	N/A
Deposited Data		
S. cerevisiae Rad51 FHA-1 structure	(Durocher et al., 2000)	PDB: 1G6G
S. cerevisiae Rad51 FHA-2 structure	(Byeon et al., 2001)	PDB: 1K2N
S. cerevisiae Dun1 FHA structure	(Lee et al., 2008)	PDB: 2JQJ
H. sapiens Chk2 FHA structure	(Li et al., 2002)	PDB: 1GXC
H. sapiens Ki67 FHA structure	(Li et al., 2004)	PDB: 1R21
H. sapiens Rnf8 FHA structure	(Huen et al., 2007)	PDB: 2PIE
M. musculus Pnk FHA structure	(Bernstein et al., 2005)	PDB: 1YJM
M. tuberculosis Rv0020c FHA structure	(Roumestand et al., 2011)	PDB: 2LC1
M. tuberculosis GarA FHA structure	(Nott et al., 2009)	PDB: 2KFU
FHA-1 crystal structure	This paper	PDB: 6CCD
FHA-2 NMR structural ensemble	This paper	PDB: 6CAH
FHA-1 chemical shifts	This paper	BMRB: 27394
FHA-2 chemical shifts	This paper	BMRB: 30399
Recombinant DNA		
Plasmid pET28-MHL	Addgene	Cat#26096
Plasmid pGEX-4T3	GE Healthcare	Cat#28954552
Plasmid pGEX-2T	GE Healthcare	Cat#28954646
Software and Algorithms		
Expasy server	(Gasteiger et al., 2005)	https://www.expasy.org/
Topspin	Bruker	https://www.bruker.com/products/mr/nmr/nmr-software/nmr-software/topspin/overview.html
NMRpipe	(Delaglio et al., 1995)	https://www.ibbr.umd.edu/nmrpipe/index.html
NMRFAM-Sparky	(Lee et al., 2015)	https://nmrfam.wisc.edu/nmrfam-sparky-distribution.htm
CYANA 3.0	(Guntert and Buchner, 2015)	http://www.cyana.org/wiki/index.php/Main_Page
MICS	(Shen and Bax, 2012)	https://spin.niddk.nih.gov/bax/software/MICS/
NMRe	(Ryu et al., 2016)	http://psb.kobic.re.kr/nmre/
Tensor2	(Dosset et al., 2000)	http://www.ibs.fr/research/scientific-output/software/tensor
Sphere	(Zhang, 1995)	http://landing.foxchase.org/research/labs/roder/sphere/
HKL2000	(Otwinowski and Minor, 1997)	http://www.hkl-xray.com/
ARP/wARP	(Langer et al., 2008)	http://www.embl-hamburg.de/ARP/
SHELXD	(Schneider and Sheldrick, 2002)	http://shelx.uni-goettingen.de/
SOLVE/RESOLVE	(Terwilliger, 2001)	https://solve.lanl.gov/
REFMAC5	(Skubak et al., 2004)	http://www.ccp4.ac.uk/html/refmac5.html

(*Continued on next page*)

Continued

REAGENT or RESOURCE	SOURCE	IDENTIFIER
Phaser	(McCoy et al., 2007)	https://www.phenix-online.org/documentation/reference/phaser.html
Phenix	(Adams et al., 2010)	https://www.phenix-online.org/
COOT	(Emsley et al., 2010)	https://www2.mrc-lmb.cam.ac.uk/personal/pemsley/coot/
PROPKA3.1	(Olsson et al., 2011)	http://propka.org/
AMBER14	(Case et al., 2014)	http://ambermd.org/
The PyMol Molecular Graphics System, Version 1.7.4.0	Schrodinger, LLC	https://pymol.org/2/
Graphpad Prism	Graphpad Software Inc.	https://www.graphpad.com/scientific-software/prism/

EXPERIMENTAL MODEL AND SUBJECT DETAILS

Escherichia coli Rosetta 2(λDE3) Singles (Novagen) were grown in LB or M9 minimal media at 37°C until induction of protein expression and at 24°C after induction. *Escherichia coli* BL21 (λDE3) Codon Plus RP cells (Invitrogen) were grown at 37°C in auto-induction media (Studier, 2005). For detailed protocols, see Method Details.

METHOD DETAILS

Protein Expression and Purification of Rv1747 Constructs for NMR Spectroscopy

Using *M. tuberculosis* H37Rv genomic DNA as a template, genes encoding $Rv1747^{1-310}$, $Rv1747^{1-156}$, $Rv1747^{206-310}$, $Rv1747^{1-213}$, $Rv1747^{148-310}$ were PCR amplified and cloned with a TAA stop codon into the pET28MHL plasmid (Addgene, plasmid #26096) via *Nde*I and *Hind*III restriction sites. Phospho-ablative threonine to alanine mutants of the Rv1747 constructs, as well as an N-terminal Trp codon in $Rv1747^{206-310}$ for quantitation, were introduced via the QuikChange site-directed mutagenesis protocol (Stratagene). After cleavage of an N-terminal His_6-affinity tag with TEV protease, two non-native residues (Gly-His) proceeded the expressed Rv1747 fragments.

Protein constructs were expressed in *Escherichia coli* Rosetta 2 (λDE3) cells in media supplemented with 35 μg/mL chloramphenicol and 35 μg/mL kanamycin. Cells were grown in LB media to produce unlabeled protein or in M9 minimal media supplemented with 3 g/L $^{13}C_6$-glucose and/or 1 g/L $^{15}NH_4Cl$ as the sole carbon and nitrogen sources, respectively, to produced uniformly labeled samples. Cultures of 1 L were incubated shaking at 37°C until $OD_{600} \sim 0.6$, induced with isopropyl-β-D-thiogalactopyranoside (IPTG; 1 mM final) and grown for another 16 hr at 24°C. After centrifugation for 15 min at 4000 g, the cell pellets were frozen at -80°C, then later thawed, resuspended in lysis buffer (20 mM sodium phosphate, 1 M NaCl, 10 mM imidazole, pH 8.0) and sonicated. After centrifugation for 1 hr at 30000 g, the supernatant was filtered (0.45 μm cutoff), applied to a Ni^{2+}-NTA HisTrap HP affinity column (GE Healthcare Life Sciences), washed with 10 column volumes of binding buffer (20 mM sodium phosphate, 500 mM NaCl, 30 mM imidazole, pH 8.0) and eluted in a 30 – 500 mM imidazole gradient. Fractions containing the desired protein were identified with SDS-PAGE, pooled and treated with His_6-tagged TEV protease while dialyzing against 4 L of cleavage buffer (20 mM sodium phosphate, 100 mM NaCl, 1 mM DTT, 0.5 mM EDTA, pH 7) for 16 hr at 4°C. Uncleaved protein, cleaved tag and TEV were removed using a second Ni^{2+}-NTA HisTrap HP affinity purification step, and the collected flow-through was concentrated and subjected to size-exclusion chromatography using a Superdex 75 (GE Healthcare Life Sciences) column with NMR sample buffer (100 mM NaCl, 20 mM sodium phosphate, pH 6.0). Final protein fractions were pooled, concentrated using a 10 kDa MWCO centrifugal filter (EMD Millipore), flash frozen and stored for further use at -80°C. Samples were verified by SDS-PAGE and electrospray ionization mass spectrometry (ESI-MS), and their concentrations determined by UV-absorbance spectroscopy using predicted ε_{280} molar absorptivities of 23950, 15470, 5500, 23950 and 8480 M^{-1} cm^{-1} for $Rv1747^{1-310}$, $Rv1747^{1-156}$, $Rv1747^{206-310}$, $Rv1747^{1-213}$ and $Rv1747^{148-310}$, respectively. All predictions were done using the Expasy server (Gasteiger et al., 2005).

Protein Expression and Purification of $Rv1747^{3-116}$ for Crystallography

Residues 3-116 of Rv1747 (FHA-1) were amplified from genomic *M. tuberculosis* DNA (strain H37Rv; obtained from TB Materials and Vaccine Testing Contract at Colorado State University) using primers designed to introduce *Bam*HI and *Eco*RI restriction sites outside the area of interest. These fragments were ligated into the plasmid pGEX-2T (GE Healthcare Life Sciences). The resulting plasmid contained amino acids for $Rv1747^{3-113}$ (FHA-1) fused to the C-terminus of GST and linked by a thrombin protease cleavage site, with the entire protein under the control of a T7 promoter. The construct was transformed and expressed in *E. coli* BL21 (λDE3) Codon Plus cells (strain RP; Stratagene). Saturated 5 mL starter cultures were used to inoculate 500 mL cultures of auto-induction medium (Studier, 2005) at a dilution of 1:1000. These 500 mL cultures were incubated for 18-24 hours at 37°C with vigorous shaking

(> 260 rpm). After centrifugation for 10 – 15 min at 5000 g, cell pellets were frozen at -20°C and then thawed and resuspended in ~ 40 mL of cold PBS buffer (140 mM NaCl, 2.7 mM KCl, 10 mM sodium phosphatte, 1.7 mM potassium phosphate, pH 7.3), containing 0.5 mM AEBSF, 5 μM E-64 and 1 μM pepstatin A, and 1 mM EDTA as protease inhibitors. Cells were lysed by sonication and the supernatant was separated by centrifugation at 17000 g. The decanted supernatant was then applied by gravity flow to an appropriate volume of Glutathione Sepharose 4 Fast Flow (GE Healthcare) equilibrated with cold PBS. After binding, the column was washed with > 10 volumes cold PBS. The GST-FHA-1 protein was eluted with 10 – 20 mM reduced glutathione (Sigma-Aldrich) in 50 mM Tris-HCL at pH 8. Fractions were collected and those containing the protein of interest were identified by SDS-PAGE, pooled, and supplemented with $CaCl_2$ to a final concentration of 1 mM. The GST-affinity-tag was then cleaved by treatment with thrombin (MP Biomedicals; 10 U protease per 1 mg GST-fusion protein) for 4 – 12 hours with gentle agitation at 4°C. The cleaved protein fragments were applied to GST-binding Sepharose equilibrated with cold PBS. The flow-through from this column was further purified by size-exclusion chromatography on a Superdex S75 column equilibrated with 50 mM NaCl, 25 mM HEPES, 0.5 mM TCEP at pH 7.8. The purified $Rv1747^{3-116}$ was concentrated and used for crystal growth.

Protein Expression and Purification of the PknF Kinase Domain

The gene encoding $Rv1746^{1-292}$ (the cytoplasmic kinase domain of PknF) was cloned from *Mtb* H37Rv genomic DNA into the pGEX-4T3 plasmid (GE Healthcare Life Sciences) with a TAA stop codon using *Bam*HI and *Xho*I restriction sites. The resulting construct, with an N-terminal glutathione S-transferase (GST) affinity tag, was expressed in *E. coli* Rosetta 2 (λDE3) cells in LB media supplemented with 35 μg/mL chloramphenicol and 100 μg/mL ampicillin. Cultures of 1 L were incubated at 37°C until OD_{600} ~ 0.6, induced with ITPG (1 mM final) and grown for another 16 hr at 24°C. After centrifugation for 15 min at 4000 g, the cell pellet was frozen at -80°C, then later thawed, resuspended in buffer (10 mM sodium phosphate, 1.8 mM potassium phosphate, 140 mM NaCl, 2.7 mM KCl, pH 7.3) and sonicated. The supernatant was centrifuged for 1 hr at 30000 g, filtered, applied to a GSTrap HP affinity column (GE Healthcare Life Sciences), washed with 10 column volumes of the same buffer, and eluted in GST elution buffer (50 mM Tris, 10 mM reduced glutathione, pH 7.4). After SDS-PAGE analysis, pooled fractions were subjected to size-exclusion chromatography using a Superdex 75 (GE Healthcare Life Sciences) column in storage buffer (100 mM NaCl, 20 mM sodium phosphate, pH 7.4). Final protein factions were pooled, concentrated using a 10 kDa MWCO centrifugal filter (EMD Millipore), flash frozen and stored for further use at -80°C. Samples were verified by SDS-PAGE and ESI-MS, and concentrations determined by UV-absorbance spectroscopy using a predicted ε_{280} = 76800 M^{-1} cm^{-1} (Gasteiger et al., 2005).

Synthetic pThr-Containing Rv1747 Peptides

Phosphorylated peptides corresponding to the reported Rv1747 modification sites at pT152 (KKYAGQQLPPA**pT**^{152}TRIPAA) and pT210 (KKYAGTEAGNLA**pT**^{210}SMMK), were purchased from Biomatik. The N-terminal acetylated and C-terminal amidated peptides were obtained in a lyophilized form after HPLC purification. These peptides, used in previously reported binding studies of the Rv1747 FHA domains (Spivey et al., 2011), include a non-native N-terminal KKYAG tag for solubility and for quantification by UV-absorbance spectroscopy (predicted ε_{280} = 1490 M^{-1} cm^{-1}) (Gasteiger et al., 2005).

In Vitro Phosphorylation of Rv1747 Constructs

Samples of Rv1747 constructs were diluted to ~ 5 μM in ~ 15 mL of buffer (20 mM sodium phosphate, 100 mM NaCl, 5 mM $MgCl_2$, pH 7.4), to which a 1:100 molar ratio of PknF:substrate protein was added directly. The bacterially expressed kinase is active, and the phosphorylation reactions were started by the addition of 5 mM ATP and incubated at 25°C with repeated inversion for 120 min. After concentration using a 10 kDa MWCO centrifugal filter (EMD Millipore), the phosphorylated samples were subjected to size-exclusion chromatography using a Superdex 75 (GE Healthcare Life Sciences) column for purification and buffer exchange (100 mM NaCl, 20 mM sodium phosphate, pH 6.0). Phosphorylation levels were ascertained using ESI-MS and phosphorylation sites confirmed indirectly from diagnostic amide $^{1}H^{N}$-^{15}N chemical shift changes.

NMR Spectroscopy

NMR spectroscopic data were recorded at 25°C on cryoprobe-equipped 500, 600 and 850 MHz Bruker Avance III spectrometers. All ^{15}N- or $^{13}C/^{15}N$-labeled samples (0.1 – 0.6 mM) were prepared in NMR buffer (100 mM NaCl, 20 mM sodium phosphate, pH 6.0) with 5 – 10 % lock D_2O, unless stated otherwise. Data were collected with Topspin (Bruker) and processed and analyzed using NMRpipe (Delaglio et al., 1995) and NMRFAM-Sparky (Lee et al., 2015), respectively. Signals from mainchain ^{1}H, ^{13}C, and ^{15}N nuclei of $Rv1747^{1-156}$ and mainchain and sidechain ^{1}H, ^{13}C, and ^{15}N nuclei of $Rv1747^{206-310}$ were assigned by standard multidimensional heteronuclear scalar correlation experiments (Sattler et al., 1999). The charge and tautomer states of the histidine sidechains of $Rv1747^{206-310}$ were determined as described previously (Platzer et al., 2014). Chemical shift-based secondary structure and RCI-S^2 predictions were performed using MICS (Shen and Bax, 2012).

NMR-Based Structure Calculations of FHA-2 ($Rv1747^{206-310}$)

The structural ensemble of $Rv1747^{206-310}$ was calculated with CYANA 3.0 (Guntert and Buchner, 2015) using chemical shift assignments, TALOS+ dihedral angle restraints (Shen and Bax, 2012), and an unassigned list of cross peaks from 3D ^{1}H–$^{15}N/^{13}C$–^{1}H NOESY–HSQC spectra (τ_{mix} = 100 ms). All X-Pro bonds were constrained to the *trans* conformation by chemical shift criteria (Schubert et al., 2002). Based on diagnostic $^{15}N^{\delta1}$ and $^{15}N^{\varepsilon2}$ chemical shifts, the histidine chains were set to the neutral $N^{\varepsilon2}H$ tautomer

for H250 and H251 and to the fully protonated imidazolium cation for H285 (Platzer et al., 2014). Seven iterations of automatic NOESY cross peak and distance restraint assignments, along with stereospecific chemical shift assignments, were carried out. At each step, an ensemble of 100 structures was calculated, followed by a final ensemble calculation from which the 20 lowest energy structures were further refined using the original NOE distance restraints, NOE-like inter-proton distance restraints from the initially calculated structures, and a knowledge based Statistical Torsion Angle Potential (STAP) in NMRe (Ryu et al., 2016). Consensus secondary structure boundaries for the Rv1747$^{206-310}$ ensemble were determined using DSSP and the figures rendered using PyMol (Schrodinger, LLC). See Table 2 for data and refinement statistics.

Backbone Amide ^{15}N Relaxation Experiments

Amide ^{15}N relaxation data (T_1, T_2 and heteronuclear NOE) were recorded for the Rv1747 protein constructs ($\sim$ 300 μM) on a cryoprobe-equipped 600 MHz Bruker Avance III spectrometer. Relaxation rate constants were determined in NMRFAM-Sparky by fitting $^{1}H^{N}$-^{15}N peak heights to a single exponential decay. The heteronuclear NOE values were determined from the ratio of the peak heights versus a control reference spectrum without ^{1}H saturation. Correlation times for global rotational diffusion were calculated with Tensor2 using these relaxation rate constants and assuming isotropic tumbling (Dosset et al., 2000).

Amide HX Measurements

Slow amide protium-deuterium HX rate constants, k_{ex}, were measured at 25°C for uniformly ^{15}N-labelled samples of $\sim$ 0.3 mM FHA-1 (Rv1747$^{1-156}$) and FHA-2 (Rv1747$^{206-310}$). The proteins in H_2O buffer (100 mM NaCl, 20 mM sodium phosphate, pH 6.0) were lyophilized and subsequently resuspended in the same volume of 99.9 % D_2O. After an initial delay of $\sim$ 6 min, successive ^{15}N-HSQC spectra were recorded with a 600 MHz spectrometer for Rv1747$^{1-156}$ (2.5 min/spectrum) and Rv1747$^{206-310}$ (5 min/spectrum), until almost all backbone amide $^{1}H^{N}$-^{15}N signals disappeared. The sample pH* values (uncorrected pH meter readings) were measured after completion of exchange, and peak heights versus time were fit to a single exponential decay with NMRFAM-Sparky (Lee et al., 2015) to obtain pseudo-first order k_{ex} rate constants. Rapid protium-protium HX was measured using the CLEANEX-PM (Hwang et al., 1998) approach with uniformly ^{15}N-labelled samples of $\sim$ 0.3 mM FHA-1 (Rv1747$^{1-156}$) and FHA-2 (Rv1747$^{206-310}$) in H_2O buffer (20 mM sodium phosphate, 100 mM NaCl, 5 % v/v D_2O lock) at 25°C and pH 6, 7 and 8. In each case, a series of 8 spectra with transfer periods ranging from 10 to 100 msec were recorded with a 600 MHz spectrometer using a recycle delay of 1.5 s Corresponding reference spectra were recorded with a recycle delay of 12 s to ensure complete water relaxation. Pseudo-first-order rate constants for exchange were obtained by nonlinear least-squares fitting of peak intensities versus transfer time. Protection factors (PF) were determined as the ratio of the intrinsic versus measured exchange rate constants. The former were predicted for a random coil polypeptide with the Rv1747 sequence and under the corresponding solvent, pH and temperature conditions using the program Sphere (Zhang, 1995). In cases where two or more reliable PF values were available from complementary measurements, these were averaged. This assumes that exchange occurs in the commonly observed EX2 limit and that the stability of the Rv1747 constructs do not change substantially over the pH range considered (Krishna et al., 2004).

NMR-Monitored Titrations

Phosphorylated peptides corresponding to pT152 or pThr210 were used in ^{15}N-HSQC-monitored titrations of FHA-1 (Rv1747$^{1-156}$) and FHA-2 (Rv1747$^{206-310}$), recorded at 25°C with a 600 MHz NMR spectrometer. Both protein and peptide samples were exhaustively dialyzed into the identical buffer (100 mM NaCl, 20 mM sodium phosphate, pH 6.0) using 3.5 – 5 kDa and 0.1 – 0.5 kDa MWCO dialysis tubing, respectively and the pH confirmed after dialysis. Aliquots of unlabeled phosphopeptide (initially $\sim$ 4.3 and 2.8 mM for pT152 and pT210, respectively) were progressively added to uniformly ^{15}N-labelled protein (initially 500 μL of $\sim$ 300 μM). Amide $^{1}H^{N}$-^{15}N chemical shift assignments of the bound proteins were extended from those of the assigned unbound proteins by tracking well resolved peaks exhibiting fast-exchange behavior over the course of the titration. The ^{1}H and ^{15}N chemical shift differences of backbone amides with respect to the unbound state, $\Delta\delta_{H,\,i}$ and $\Delta\delta_{N,\,i}$, respectively, were monitored and the overall chemical shift perturbations (CSP) $\Delta\delta_i$ at each titration point i were calculated as $\Delta\delta_i = [(0.14\Delta\delta_{N,\,i})^2 + (\Delta\delta_{H,\,i})^2]^{1/2}$. The resulting titration curves for individual amides were non-linear least squares fit in GraphPad Prism to the equation for a 1:1 binding isotherm,

$$\Delta\delta_i = \Delta\delta_{sat}\,\frac{\left([P]_{T,i} + [L]_{T,i} + K_d\right) - \sqrt{\left([P]_{T,i} + [L]_{T,i} + K_d\right)^2 - 4[P]_{T,i}[L]_{T,i}}}{2[P]_{T,i}}$$

where $[P]_{T,\,i}$ and $[L]_{T,\,i}$ are the dilution-corrected concentrations of protein and peptide, respectively at each titration point i, K_d is the fit equilibrium dissociation constant, and $\Delta\delta_{sat}$ is the extrapolated chemical shift perturbation at saturation. The reported K_d values and the associated standard deviations were determined by averaging the fit values of the six most perturbed amides for each of the four FHA/peptide combinations.

Crystallization of Rvl747$^{3-116}$

Preliminary crystals were obtained at 18°C via the microbatch technique using 10 mg/mL protein and the Wizard I screen, condition 08 (2 M ammonium phosphate, 100 mM citrate buffer, pH 5.5) with 10% silicon, 90% paraffin overlay. Optimal crystals were obtained

via the same microbatch approach with an initial protein concentration of 18 mg/mL in 1.8 M ammonium sulfate, 100 mM citrate buffer, pH 5.5. These were single, rod-shaped crystals of approximately 0.4 mm length that diffracted to < 2 Å resolution when soaked in n-paratone oil and flash frozen in liquid nitrogen. They indexed to a primitive trigonal space group, and contained one molecule in the asymmetric unit (Table 1). Heavy atom-bound crystals were obtained by a short incubation (30 – 60 seconds) in cryoprotectant containing 0.5 M NaBr, 1 M ammonium sulfate, 100 mM citrate pH 5.5, and 25 % ethylene glycol, followed by flash-freezing in liquid nitrogen.

X-ray Crystallography Data Collection, Processing, and Structure Determination of FHA-1 (Rvl747$^{3\text{-}116}$)

X-ray data were collected on beamline 8.3.1 at the Advanced Light Source at Lawrence Berkeley National Laboratory. Data were integrated and scaled using the program HKL2000 (Otwinowski and Minor, 1997). Seven bromide ions were identified in a crystal frozen in cryoprotectant containing 0.5 M NaBr via multi-wavelength anomalous diffraction (MAD) analysis with SHELXD (Schneider and Sheldrick, 2002) of data collected at wavelengths 0.9200 Å, 0.9202 Å, and 1.1159 Å. Further analysis with SOLVE/RESOLVE (Terwilliger, 2001) generated two bromide sites. These proved sufficient to calculate accurate phases and produce an interpretable electron density map. ARP/wARP (Langer et al., 2008) was used to build a partial C^{α} backbone into this density, and the remainder of the backbone trace was completed by hand. This preliminary model was improved through iterative cycles of restrained refinement with REFMAC5 (Skubak et al., 2004) and manual rebuilding until the R_{cryst} and R_{free} were 0.21 and 0.25, respectively. The model was used to calculate phases for the highest resolution data set (1.8 Å) collected a native crystal without bromide. Molecular replacement solutions were generated using Phaser (McCoy et al., 2007), refined with PHENIX (Adams et al., 2010) and rebuilt in COOT (Emsley et al., 2010). See Table 1 for data and refinement statistics.

Isothermal Titration Calorimetry

Isothermal titration calorimetry (ITC) studies were carried out at 25°C using a MicroCal ITC200 (GE Healthcare Life Sciences). Protein and peptide samples were exhaustively dialyzed into the identical buffer (100 mM NaCl, 20 mM sodium phosphate, pH 6.0 or pH 8.0) using 3.5 – 5 kDa and 0.1 – 0.5 kDa MWCO dialysis tubing, respectively and the pH confirmed after dialysis. Phosphorylated peptides corresponding to pT152 or pThr210 (initially ~ 4.3 and 2.8 mM, respectively, ~ 30 uL added) were titrated in a stepwise manner into solutions of FHA-1 (Rv1747$^{1\text{-}156}$) and FHA-2 (Rv1747$^{206\text{-}310}$), initially at ~ 0.5 and 0.2 mM, respectively. Dilution heats were determined by repeating the same titrations of peptide into buffer and subsequently subtracted from the data to obtain the final corrected binding heats. These titration data were then fit to a 1:1 binding model using Origin (GE Healthcare Life Sciences). Protein concentrations were adjusted to yield a stoichiometry value n =1. This accounts for loss in binding activity or errors in the concentrations of the proteins or phosphopeptides determined using predicted ε_{280} values. Thermodynamic parameters are only reported for FHA-2 as the uncertainties associated with fitting the FHA-1 isotherms are large due to weak binding and low enthalpy changes.

Circular Dichroism Spectroscopy

Circular dichroism (CD) spectra were recorded for ~ 10 μM FHA-1 (Rv1747$^{1\text{-}156}$) and FHA-2 (Rv1747$^{206\text{-}310}$) at 25°C using a JASCO J-810 spectropolarimeter. Data were measured between 210 nm to 280 nm using a 100 nm/min scan rate, 100 mdeg sensitivity and 0.1 s response time. The proteins were in buffer (100 mM NaCl, 20 mM sodium phosphate, pH 6.0) with 0 – 5 M guanidinium hydrochloride (GuHCl; SIGMA ≥99%, recrystallized). The GuHCl concentrations were determined by refractive index (Pace et al., 1989). Ellipticity values, θ, at 217 nm and 217.5 nm for FHA-1 and FHA-2, respectively, versus [GuHCl] were fit for a two-state unfolding transition using GraphPad Prism according to the following equations,

$$\theta = \theta_{f_0} + [GuHCl]s_f + f_u\left(\theta_{u_0} + [GuHCl]s_u - \theta_{f_0} - [GuHCl]s_f\right)$$

$$f_u = \frac{K_u}{1 + K_u}$$

$$K_u = e^{-\Delta G_u/RT}$$

$$\Delta G_u = \Delta G_{u,\,H_2O} - m[GuHCl]$$

where s_f and s_u denote the slopes of the θ dependence on [GuHCl] for the fully folded and unfolded proteins, respectively and θ_{f_0} and θ_{u_0} are their extrapolated y-intercepts, f_u is the fraction of unfolded protein, K_u the equilibrium constant for the unfolding transition and ΔG_u the corresponding difference in free energy between unfolded and folded protein at a certain [GuHCl]. $\Delta G_{u,H_2O}$ is the free energy difference between unfolded and folded protein at [GuHCl] = 0 M and m is the slope of the assumed linear ΔG_u vs [GuHCl] dependence (Pace et al., 1989).

Molecular Dynamics Simulations

Molecular dynamics (MD) simulations were carried using X-ray crystallographic structure of FHA-1 and the lowest energy member of the NMR-derived structural ensemble of FHA-2. Both were truncated to the core residues for FHA-1 (8 – 105) and FHA-2 (225 – 310). PROPKA3.1 (Olsson et al., 2011) was used to predict protonation states at pH 7. Both proteins were solvated in a cuboid explicit

TIP3P water box and 4 Na^+ ions were added to FHA-2 to neutralize the system. The final number of atoms were 17189 and 18950 for FHA-1 and FHA-2, respectively, and the box dimensions were 59.0 Å·62.0 Å·59.6 Å and 65.3 Å·58.5 Å·63.1 Å. After 5000 steps of steepest descent energy minimization of the solvent with the protein coordinates fixed, and an additional 10000 steps for all atoms including the protein, the systems were heated to 300 K over 50 ps and 1 ns of equilibration was performed. The production run of a total of 900 ns of Langevin dynamics was performed with an integration step size of 2 fs in the modified AMBER ff14SB all-atom force field using the PREMD module in AMBER14 (Case et al., 2014). The isobaric isothermal ensemble was used at 300 K and a pressure of 1 atm with periodic boundary conditions and the long range electrostatic interactions were accounted for using the particle-mesh Ewald sum. A cutoff of 10 Å was used for long-range non-bonded interactions. The SHAKE algorithm was used to constrain bonds involving hydrogens. Backbone (N, C^{α}, CO) RMSD time courses were calculated from the trajectories aligned to the starting crystal and NMR structures as well as the solvated, equilibrated structures using CPPTRAJ, a module of AMBER14. This module was further used to calculate the per-residue backbone (N, C^{α}, CO) RMS fluctuations and they were mapped onto the structures and visualized using PyMol (Schrodinger, LLC).

Structural Alignment

Structures of previously reported FHA domains (*S. cerevisiae* Rad51 FHA-1, PDB ID 1G6G.pdb; *S. cerevisiae* Rad51 FHA-2, 1K2N.pdb; *S. cerevisiae* Dun1, 2JQJ.pdb; *H. sapiens* Chk2, 1GXC.pdb; *H. sapiens* Ki67, 1R21.pdb; *H. sapiens* Rnf8, 2PIE.pdb; *M. musculus* Pnk, 1YJM.pdb; *M. tuberculosis* Rv0020c, 2LC1.pdb; *M. tuberculosis* GarA, 2KFU.pdb), as well as the lowest energy structure of the NMR determined ensemble of Rv1747 FHA-2, were aligned to Rv1747 FHA-1 using CE-CP, an incremental combinatorial extension approach that was optimized for comparison of circularly permuted protein structures (Shindyalov and Bourne, 1998).

QUANTIFICATION AND STATISTICAL ANALYSIS

Chemical shift perturbations of NMR interaction studies were least square fit using GraphPad Prism to a 1:1 binding isotherm. Mean binding constants and the associated standard deviations were determined by averaging the six most perturbed amides. For ITC interaction studies, K_d, ΔH and the stoichiometry value n were fit using a 1:1 binding model in Origin (GE Healthcare Life Sciences). ΔS was then calculated from these fitted values and the uncertainties of the fit are reported for all. CD ellipticity traces of chemical unfolding studies using GuHCl were least square fit for a two-state unfolding transition in GraphPad Prism. The fit values of $\Delta G_{u,\,H_2O}$ and m and the associated uncertainties are reported.

DATA AND SOFTWARE AVAILABILITY

The coordinates and X-ray crystallographic structure factors for $Rvl747^{3\text{-}116}$ (FHA-1) have been deposited in the Protein Data Bank (http://www.rcsb.org) under ID code 6CCD. The coordinates and NMR-derived restraints for the $Rv1747^{206\text{-}310}$ (FHA-2) ensemble have deposited as 6CAH. The chemical shift assignments for $Rv1747^{1\text{-}156}$ (FHA-1) and $Rv1747^{206\text{-}310}$ (FHA-2) have been deposited in the Biological Magnetic Resonance Bank (http://www.bmrb.wisc.edu/) as 27394 and 30399, respectively.

Structure, Volume *26*

Supplemental Information

Biophysical Characterization of the Tandem FHA Domain Regulatory Module from the *Mycobacterium tuberculosis* ABC Transporter Rv1747

Florian Heinkel, Leo Shen, Melissa Richard-Greenblatt, Mark Okon, Jennifer M. Bui, Christine L. Gee, Laurie M. Gay, Tom Alber, Yossef Av-Gay, Jörg Gsponer, and Lawrence P. McIntosh

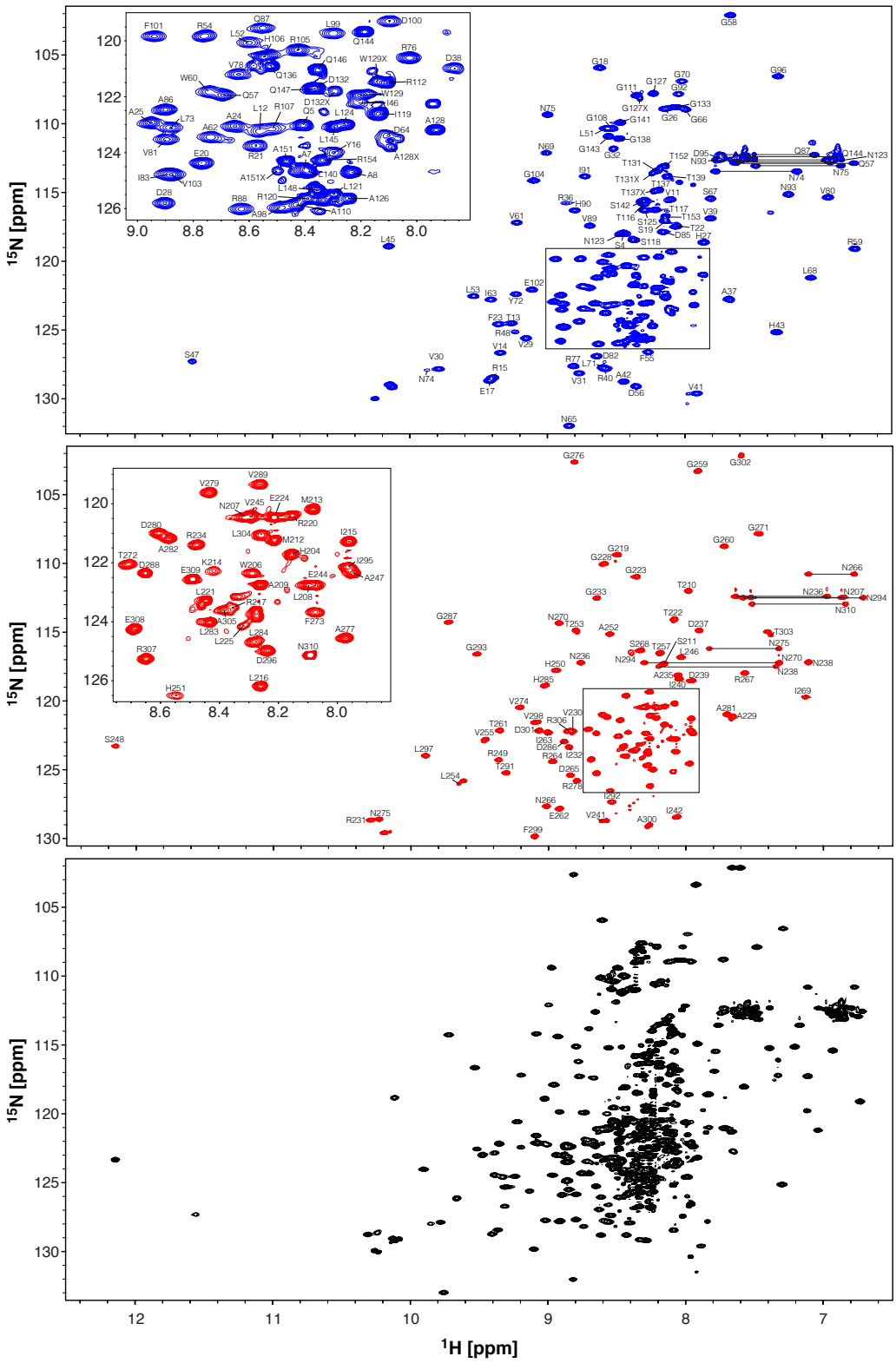

Figure S1 ***(related to Figure 2)***
Assigned ^{15}N-HSQC spectra of the (A) FHA-1 (Rv1747$^{1\text{-}156}$) and (B) FHA-2 (Rv1747$^{206\text{-}310}$) constructs (25 ^{o}C, 100 mM NaCl, 20 mM sodium phosphate, pH 6.0). (C) Also shown is the spectrum of the full FHA regulatory domain (Rv1747$^{1\text{-}301}$). These spectra are superimposed in Figure 2B.

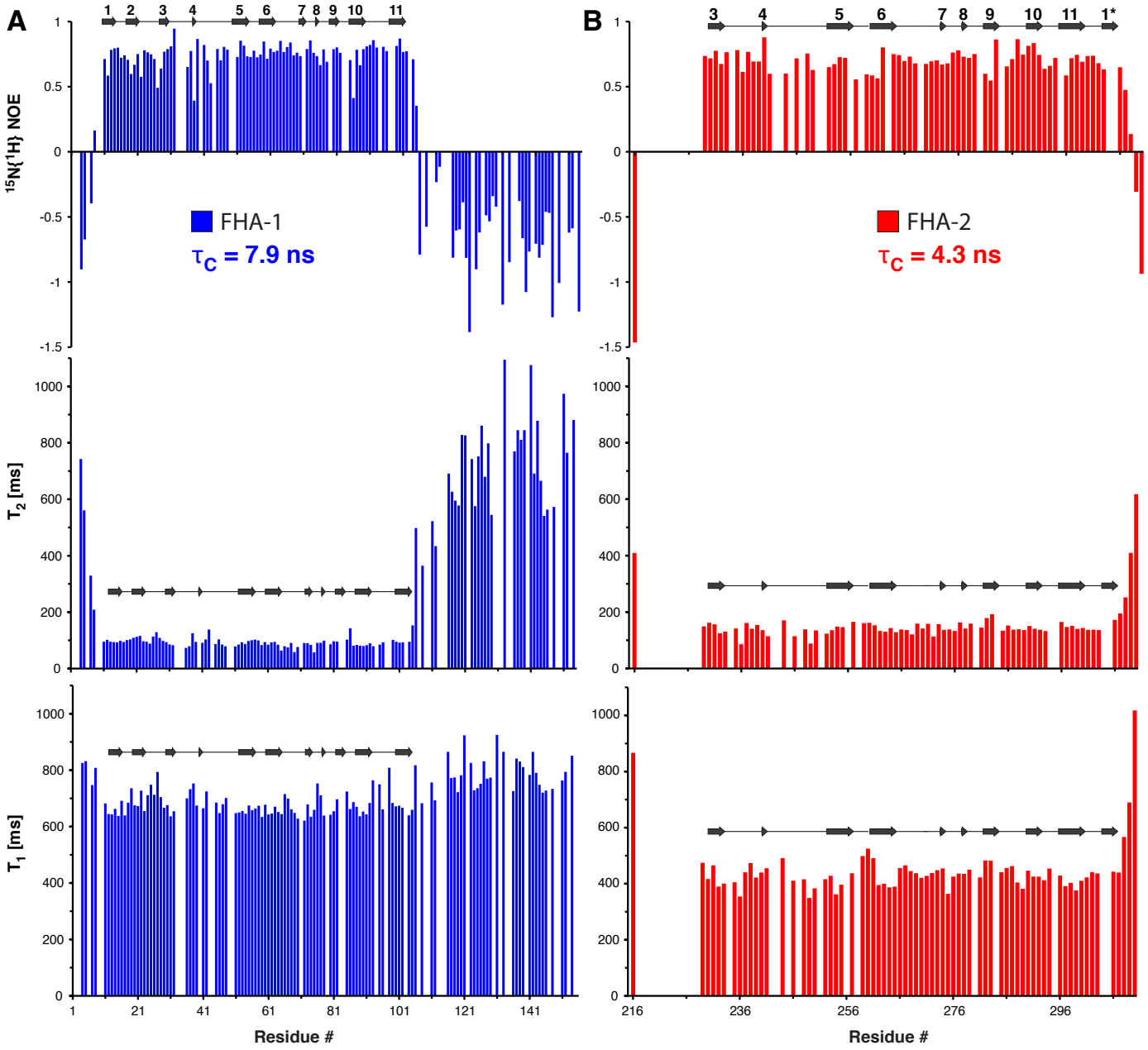

Figure S2 ***(related to Figure 2)***

Amide ^{15}N relaxation data (T_1, T_2, and heteronuclear NOE) for the FHA-1 ($Rv1747^{1-156}$, blue) and FHA-2 ($Rv1747^{206-310}$, red) constructs, recorded with a 600 MHz NMR spectrometer (25 ^oC, 100 mM NaCl, 20 mM sodium phosphate, pH 6.0). The correlation times for isotropic global rotational diffusion (τ_c) were determined from the T_1 and T_2 values for ordered FHA domain residues using Tensor2 (Dosset et al., 2000). These residues exhibit relatively uniform relaxation parameters with heteronuclear NOE values ~ 0.8, indicative of restricted fast timescale motions. In contrast, the conformationally disordered terminal and ID linker residues have negative heteronuclear NOE values and long T_2 lifetimes due to sub-nsec timescale motions. Secondary structures calculated with DSSP are indicated (arrow, β-strand). Missing data points correspond to prolines and amides with overlapping or unassigned signals.

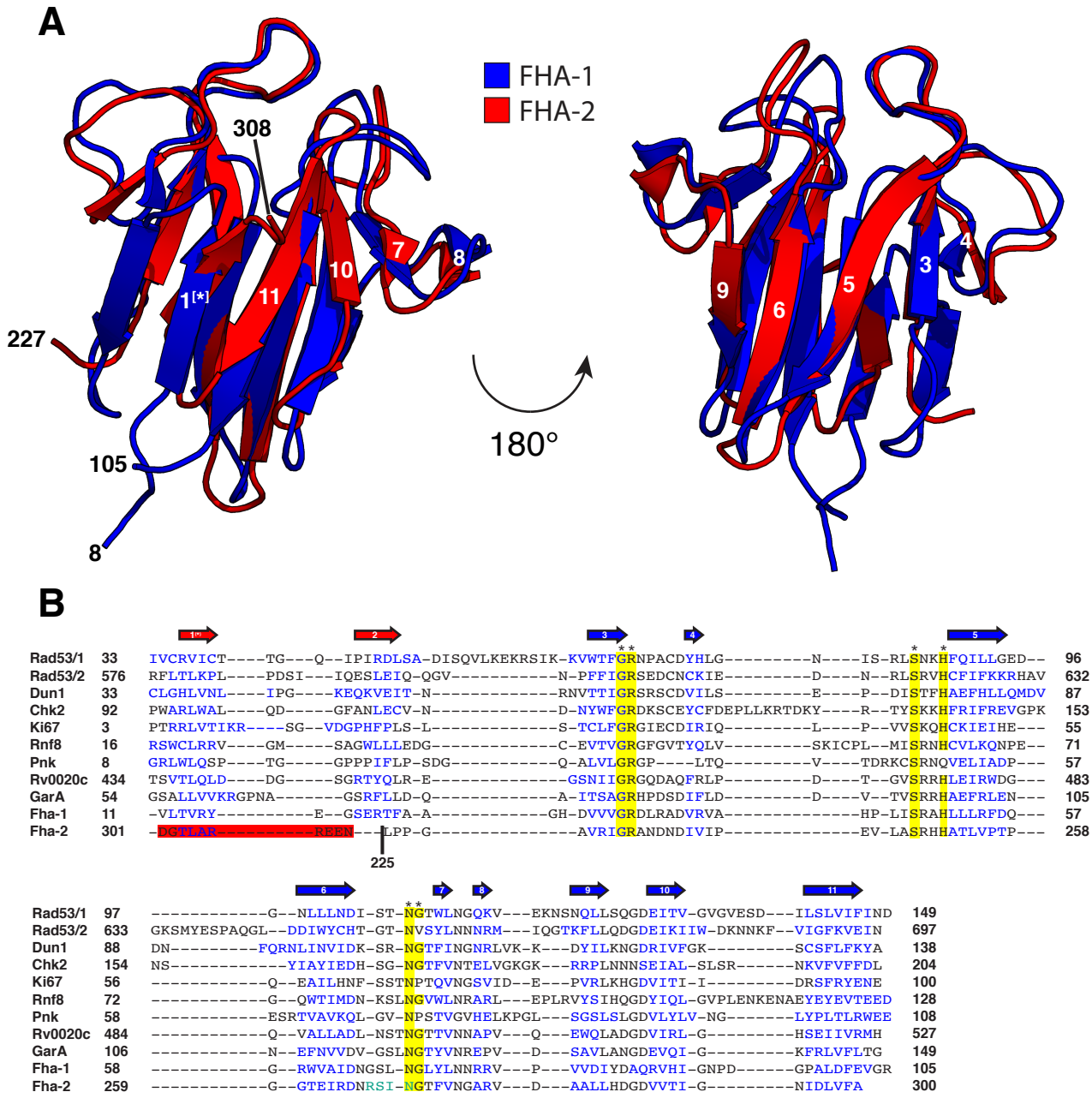

Figure S3 ***(related to Figure 3)***

(A) Alignment of the X-ray crystallographic structure of FHA-1 (blue) and the lowest energy member of the NMR-derived structural ensemble of FHA-2 (red). The RMSD for all mainchain atoms, including those in loop regions, is 1.4 Å. (B) Structure-based sequence alignment of FHA domains generated with the RCSB PDB jCE server (https://www.rcsb.org/). Conserved residues that interact with the bound peptide are highlighted in yellow and with an asterisk. Residues in β-strands are in blue font. The circularly permutated residues of Rv1747 FHA-2 are highlighted in red. (*S. cerevisiae* Rad51 FHA-1, PDB ID 1G6G.pdb; *S. cerevisiae* Rad51 FHA-2, 1K2N.pdb; S. *cerevisiae* Dun1, 2JQJ.pdb; *H. sapiens* Chk2, 1GXC.pdb; *H. sapiens* Ki67, 1R21.pdb; *H. sapiens* Rnf8, 2PIE.pdb; *M. musculus* Pnk, 1YJM.pdb; *M. tuberculosis* Rv0020c, 2LC1.pdb; *M. tuberculosis* GarA, 2KFU.pdb; *M. tuberculosis* FHA-1; *M. tuberculosis* FHA-2).

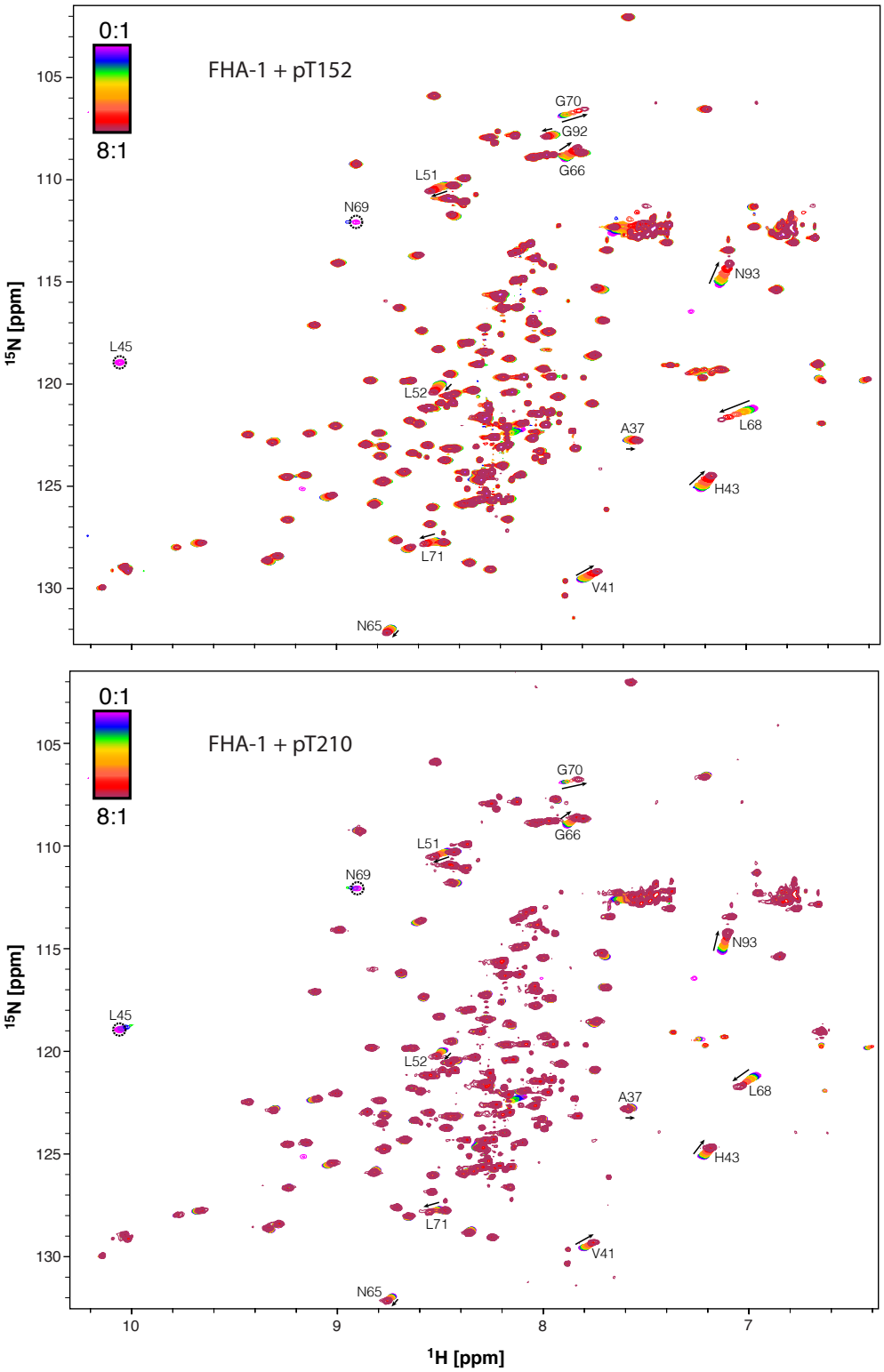

Figure S4 ***(related to Figure 4)***

Overlaid spectra from ^{15}N-HSQC monitored titrations of ^{15}N-labeled FHA-1 (Rv1747$^{1\text{-}156}$) with unlabeled synthetic phosphorylated peptide models of the pT152 and pT210 phospho-acceptor sites. The peptide:protein ratios are indicated with a rainbow color gradient. The progressive shift changes of selected amides showing binding in the fast exchange limit are shown by arrows. Amides exhibiting severe intermediate exchange broadening are identified with dashed circles.

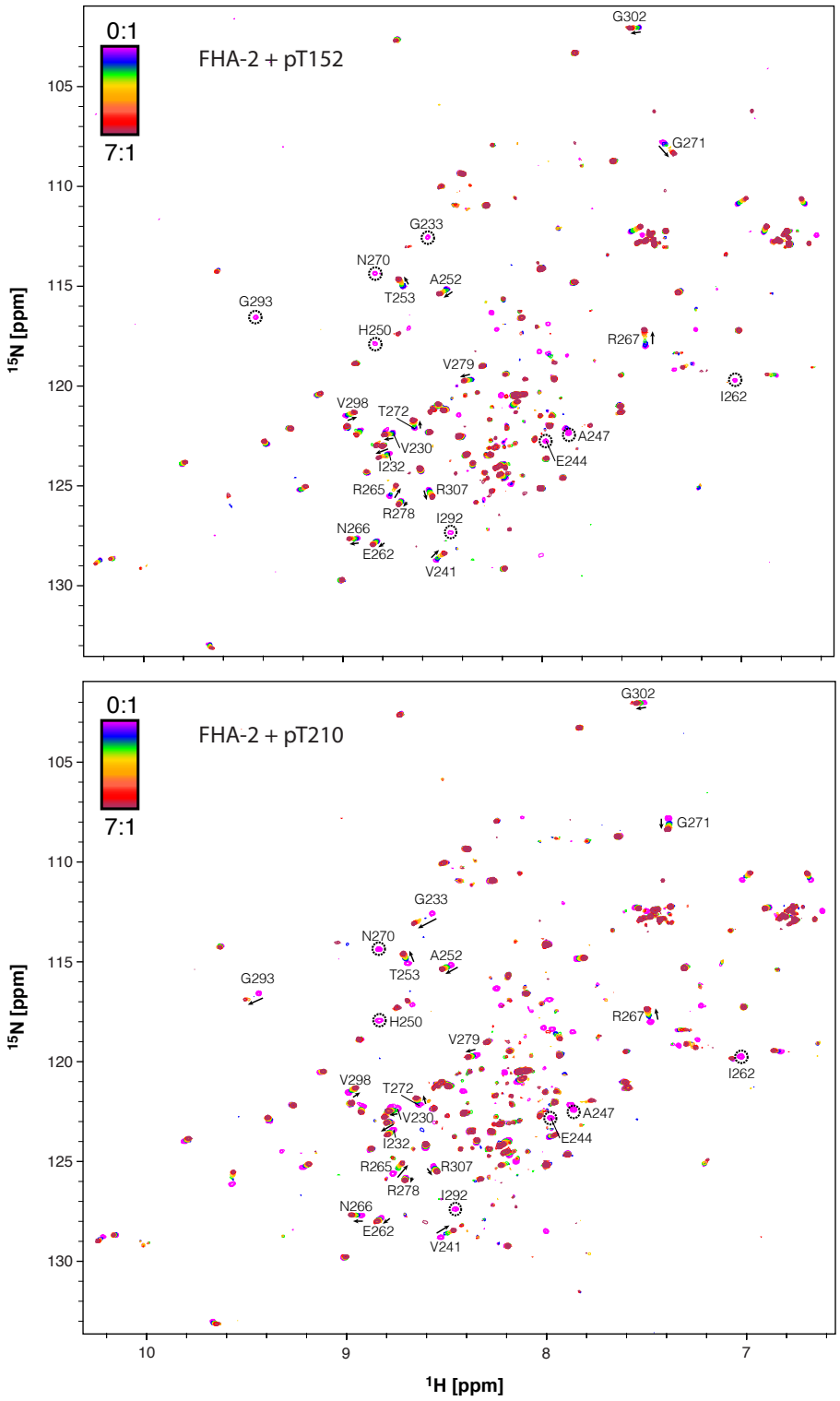

Figure S5 ***(related to Figure 4)***

Overlaid spectra from ^{15}N-HSQC monitored titrations of ^{15}N-labeled FHA-2 (Rv1747$^{206-310}$) with unlabeled synthetic phosphorylated peptide models of the pT152 and pT210 phospho-acceptor sites. The peptide:protein ratios are indicated with a rainbow color gradient. The progressive shift changes of selected amides showing binding in the fast exchange limit are shown by arrows. Amides exhibiting severe intermediate exchange broadening are identified with dashed circles.

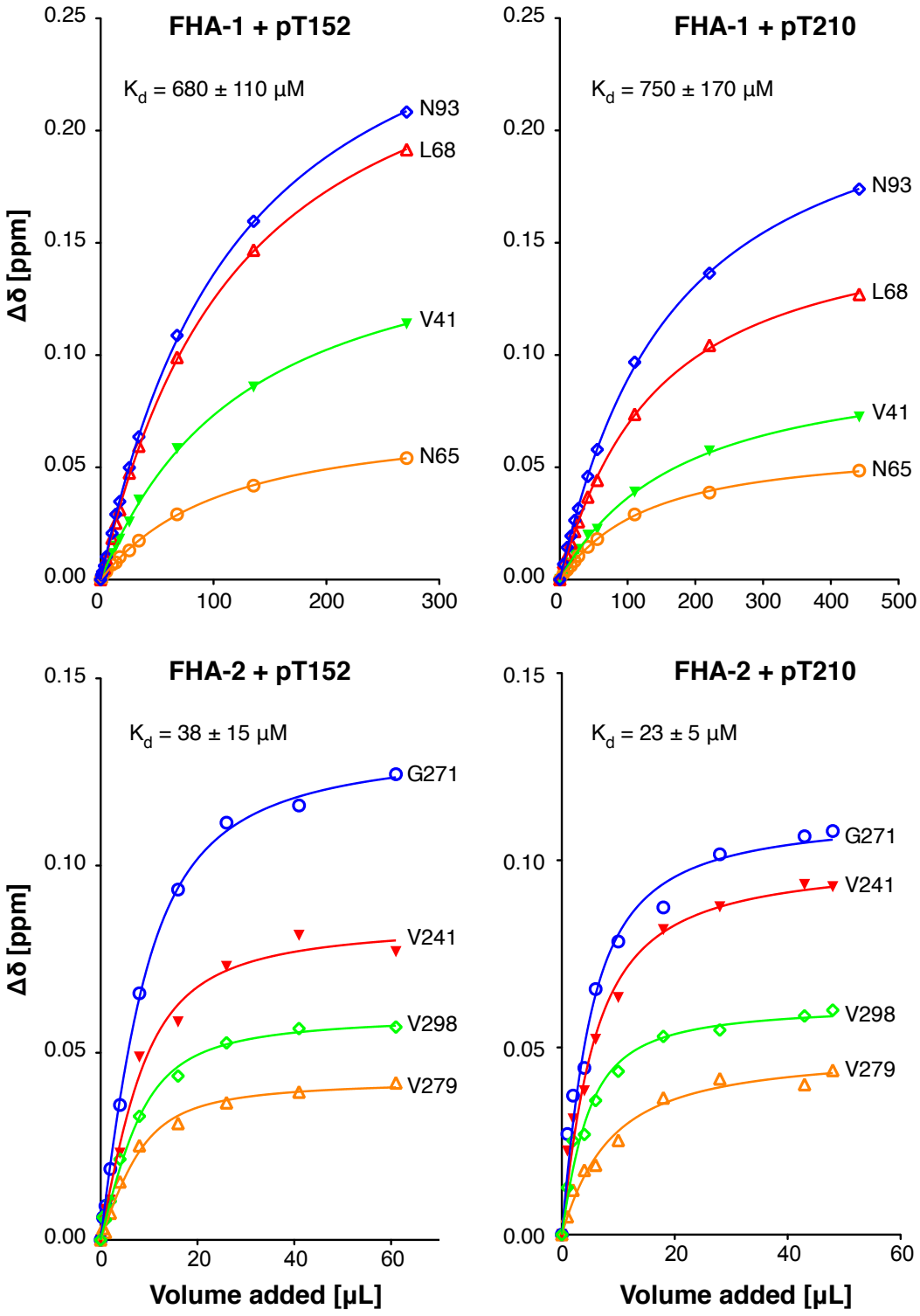

Figure S6 ***(related to Figure 4 and Table 3)***
Representative binding isotherms for the NMR-monitored titrations of FHA-1 ($Rv1747^{1-156}$) and FHA-2 ($Rv1747^{206-310}$) with peptides corresponding to the pT152 and pT210 phospho-acceptor sites (25 ^{o}C, 100 mM NaCl, 20 mM sodium phosphate, pH 6.0). The lines are best individual fits to a 1:1 binding isotherm, with the resulting K_d values averaged for Table 3. See Figures 4A, S4 and S5 for corresponding spectra, and Methods for experimental details.

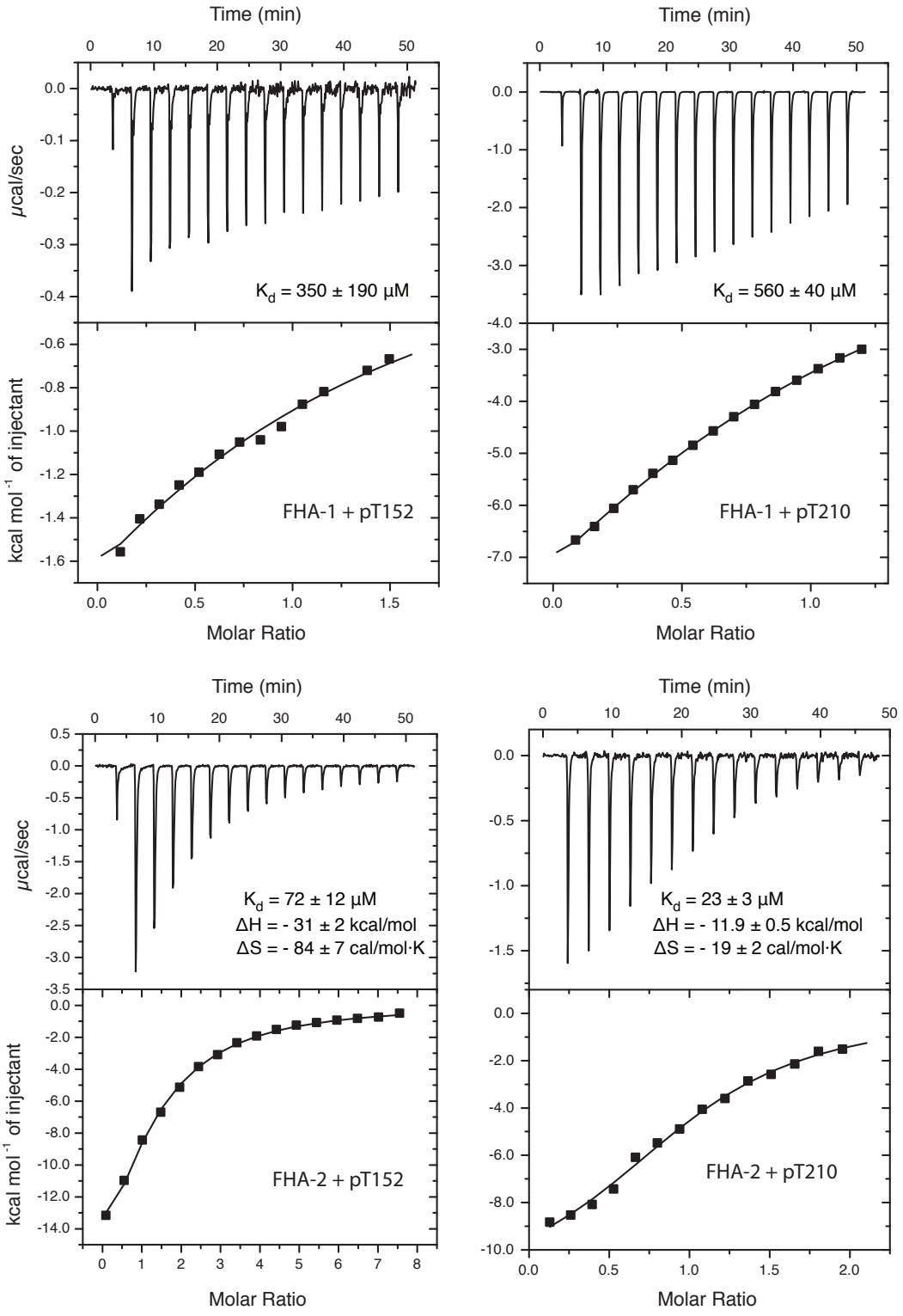

Figure S7 ***(related to Table 3)***

Isothermal titration calorimetry data for titrations of FHA-1 ($Rv1747^{1-156}$) and FHA-2 ($Rv1747^{206-310}$) with peptides corresponding to the pT152 and pT210 phospho-acceptor sites (25 ^{o}C , 100 mM NaCl, 20 mM sodium phosphate, pH 6.0). The baseline corrected data were fit to a 1:1 binding isotherm, with protein concentrations adjusted to obtain this stoichiometry. See Methods for experimental details.

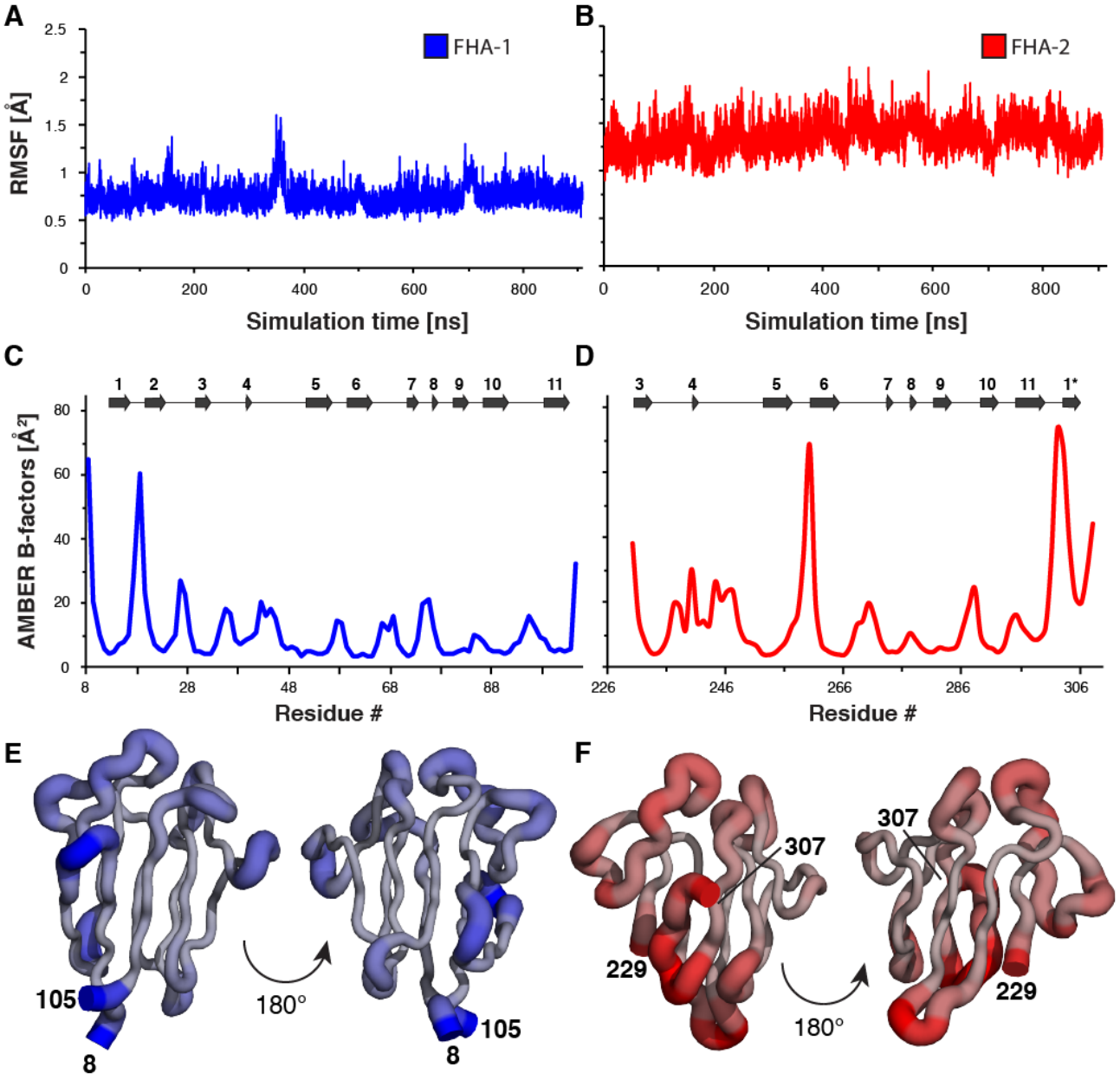

Figure S8 ***(related to Figures 4 and 5)***
Backbone (N, C^{α}, CO) RMS fluctuations of (A) FHA-1 ($Rv1747^{8-105}$) and (B) FHA-2 ($Rv1747^{225-310}$) over a 900 ns AMBER MD simulation with solvation in an explicit water model. Both domains remained stable with average RMSFs from the corresponding experimental structures of only 0.75 Å and 1.35 Å, respectively. Backbone AMBER B-factors, back-calculated from 900 ns MD simulations of (C, E) FHA-1 and (D, F) FHA-2. Higher values are indicated on the corresponding structures by a thicker backbone and by a grey-blue or grey-red gradient.

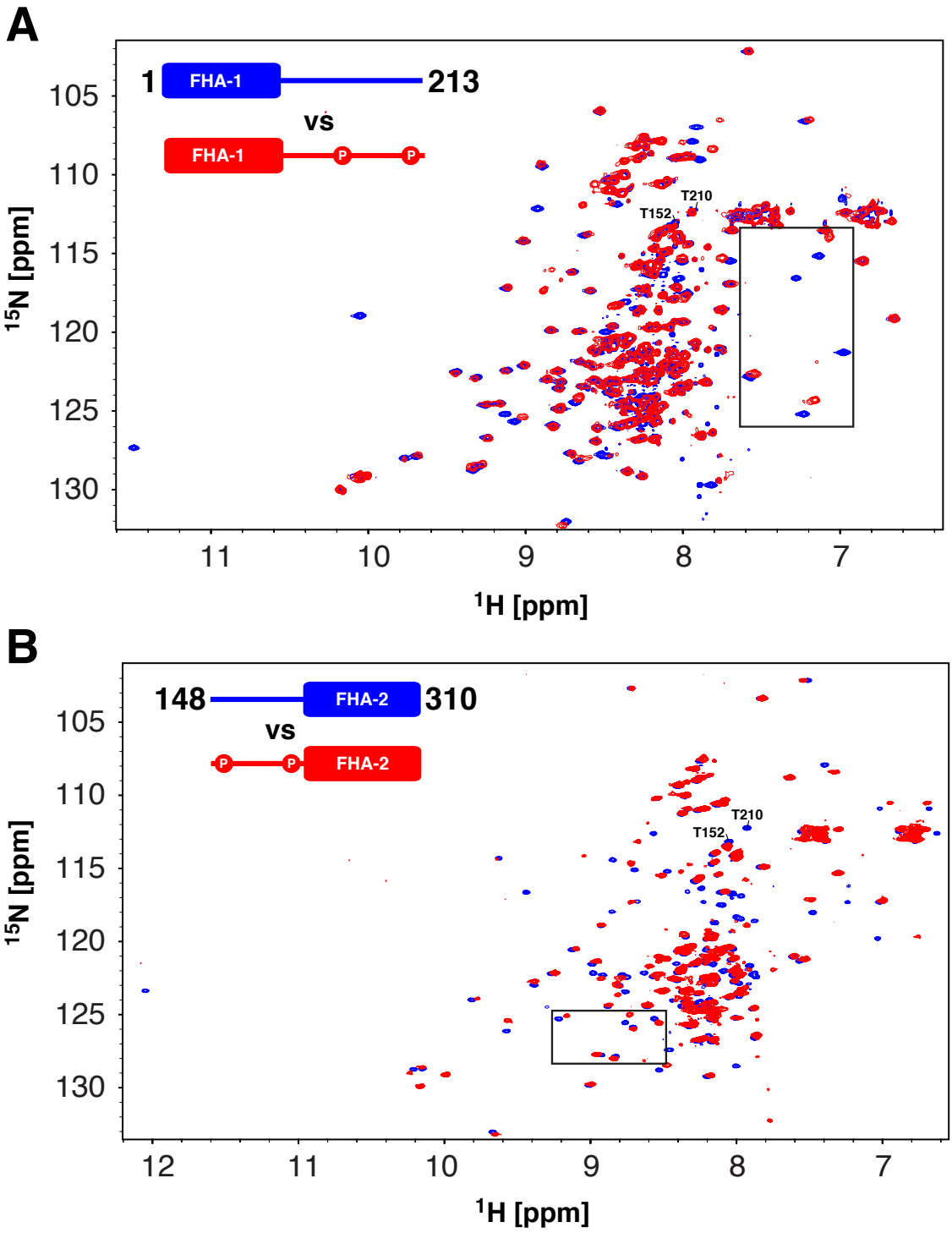

Figure S9 ***(related to Figure 6)***
Overlaid ^{15}N-HSQC spectra of ^{15}N-labeled FHA-1 (Rv1747$^{1\text{-}213}$; top) and FHA-2 (Rv1747$^{148\text{-}310}$; bottom) with the linker residues T152 and T210 unmodified (blue) and phosphorylated by PknF (red). Although partially obscured by spectral overlap, the $^{1}H^{N}$-^{15}N signals of T152 and T210 shift to unassigned chemical shifts upon phosphorylation. Additional changes in chemical shift and signal intensity (exchange broadening and increased molecular mass) result from inter- and intramolecular FHA-pThr interactions. The boxed regions are expanded in Figures 6C,F.

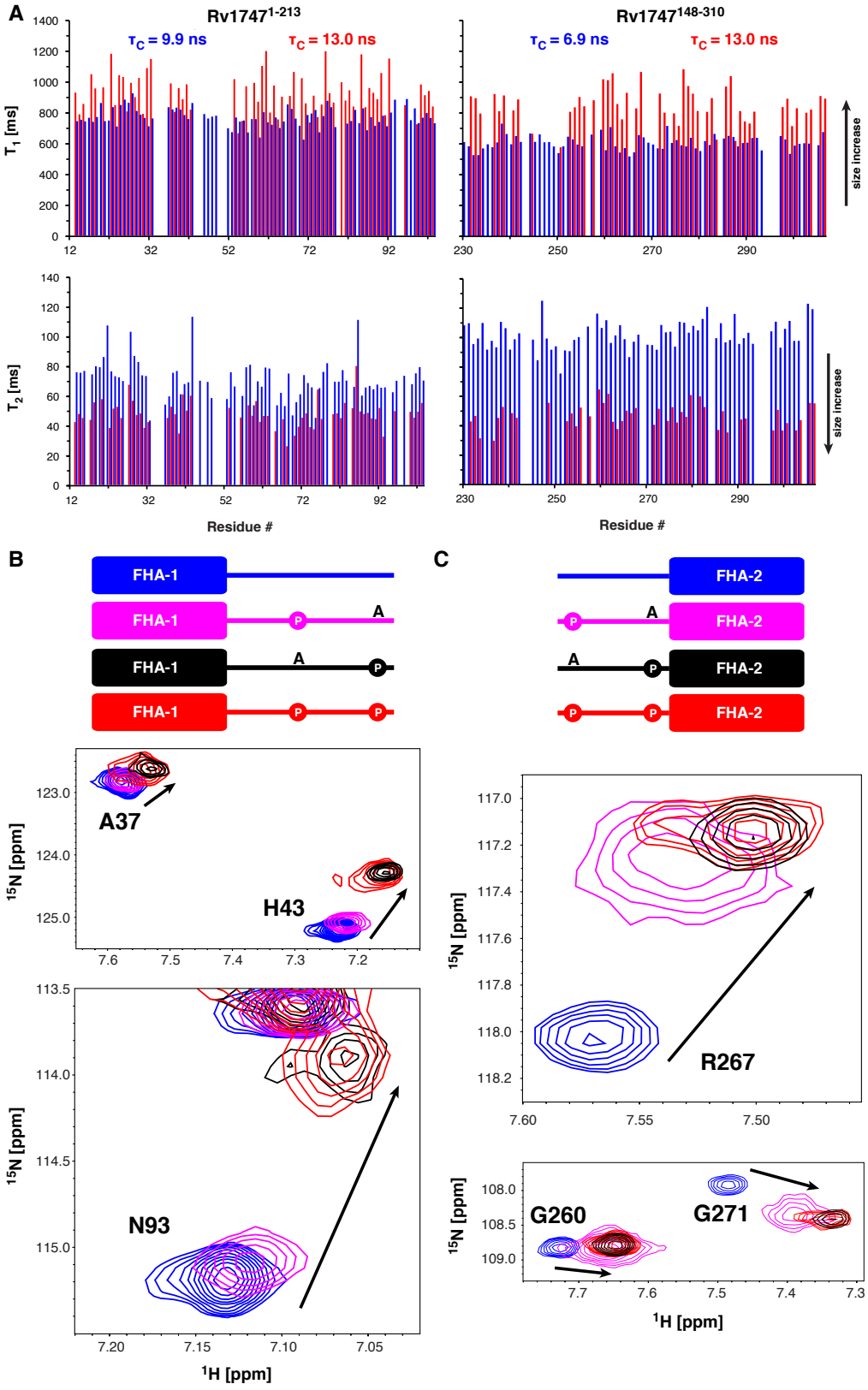

Figure S10 ***(related to Figure 6)***

(A) Phosphorylation of the linker residues T152 and T210 in the FHA-1 (Rv1747$^{1-213}$) and FHA-2 (Rv1747$^{148-310}$) constructs leads to oligomerization. Shown are the amide ^{15}N T_1 and T_2 lifetimes of the

two constructs in their unmodified (blue) and dual phosphorylated (red) forms. The increased T_1 and decreased T_2 values of the phosphorylated species indicate slower rotational diffusion (longer isotropic correlation times τ_C for global tumbling) due to FHA-pThr mediated association. The two constructs differ in polypeptide chain length (213 versus 162 residues, respectively) and hence in relative relaxation lifetimes. Overlaid regions of ^{15}N-HSQC spectra of uniformly ^{15}N-labeled (B) FHA-1 (Rv1747$^{1\text{-}213}$) and (C) FHA-2 (Rv1747$^{148\text{-}310}$) show differential effects of phosphorylation. Peaks from the unmodified wild-type proteins are in blue, from the T210A mutants with single phosphorylation at pT152 in pink, from the T152A mutants with single phosphorylation at pT210 in black, and from the wild-type proteins with dual phosphorylation at pT152 and pT210 in red. The directions of progressive chemical perturbation upon increased FHA-pThr binding are indicated with arrows.